Structural basis of rotavirus RNA chaperone displacement and RNA annealing

Jack P. K. Bravo[1,2,†] Kira Bartnik[3], Luca Venditti[1], Emma H. Gail[4,5], Chen Davidovich[4,5], Don C Lamb[3], Roman Tuma[2,6], Antonio N. Calabrese[2], Alexander Borodavka*[1,2,3]

1. Department of Biochemistry, University of Cambridge, 8 Tennis Court Road, Cambridge, CB2 1QW, UK
2. Astbury Centre for Structural Molecular Biology, School of Molecular and Cellular Biology, Faculty of Biological Sciences, University of Leeds, Leeds, UK
3. Department of Chemistry, Center for NanoScience (CeNS), Nanosystems Initiative Munich (NIM) and Centre for Integrated Protein Science Munich (CiPSM), Ludwig Maximilian University of Munich, Munich, Germany
4. Department of Biochemistry and Molecular Biology, Biomedicine Discovery Institute, Faculty of Medicine, Nursing and Health Sciences, Monash University, Clayton, Victoria, Australia
5. EMBL-Australia and the ARC Centre of Excellence in Advanced Molecular Imaging, Clayton, Victoria, Australia
6. Faculty of Science, University of South Bohemia, Ceske Budejovice, Czech Republic

* To whom correspondence should be addressed.

† Current address: Department of Molecular Biosciences, University of Texas at Austin, Austin, Texas 78712-1597, USA

Abstract

Rotavirus genomes are distributed between 11 distinct RNA segments, all of which are essential for virus replication. Stoichiometric genome segment selection and assembly is achieved through a series of sequence-specific, intersegment RNA-RNA interactions that are facilitated by the rotavirus RNA chaperone protein NSP2. The C-terminal region (CTR) of NSP2 has been proposed to play a role in rotavirus replication, although its mechanistic contribution to the RNA chaperone activity of NSP2 remained unknown. Here, we use single-molecule fluorescence assays to directly demonstrate that the CTR is required for promoting RNA-RNA interactions and that it limits the RNA unwinding activity of NSP2. Unexpectedly, hydrogen-deuterium exchange-mass spectrometry and UV-crosslinking data indicate that the CTR does not interact with RNA. However, removal of the CTR reduced the RNA release activity of NSP2, suggesting that the CTR is important for chaperone recycling. To further interrogate the role of the CTR, we determined cryo-EM structures of NSP2 and its ribonucleoprotein complexes. These reveal that although the CTR is ampholytic in nature, it harbours a highly conserved acidic patch that is poised towards bound RNA. Using a reverse genetics approach, we demonstrate that rotavirus mutants harbouring triple alanine mutations within the acidic patch failed to replicate, while mutations that preserve the charge of the CTR successfully restored viral replication. Together, our data suggest that the CTR reduces the accumulation of kinetically trapped NSP2-RNA complexes by accelerating RNA dissociation via charge repulsion, thus promoting efficient intermolecular RNA-RNA interactions during segment assembly.

Introduction

Selective incorporation of viral genomes into nascent virions is essential for virus replication. This process is highly challenging for RNA viruses with multi-segmented genomes (including rotaviruses) since they must coordinate the selection and assembly of 11 distinct RNAs (*1*, *2*). Despite these challenges, rotaviruses achieve highly efficient, selective and stoichiometric genome assembly through a series of redundant, sequence-specific intermolecular RNA-RNA contacts (*3*). While RNA-RNA interactions may underpin genome assembly, the remarkable selectivity of these interactions is determined by a complex network of RNA-protein interactions (*4*). In rotaviruses (RV), the viral RNA chaperone protein NSP2 facilitates sequence-specific intersegment RNA-RNA interactions to ensure robust assembly of complete viral genomes (*5*, *6*).

NSP2 is a multivalent, non-specific RNA chaperone with high nM affinity for ssRNA (*4*, *7*). This allows it to both act as a matchmaker of intermolecular duplexes and limit transient, non-specific RNA-RNA interactions (*4*, *8*). This creates a mechanistic conundrum, as NSP2 has to balance helix unwinding and RNA annealing in order to achieve accurate and stoichiometric assembly of distinct RNAs. As such, this viral RNA chaperone plays an absolutely critical role in RV replication (*9*, *10*).

Previous mutational studies of NSP2 have been hindered by the lack of a robust reverse genetics system (*11–13*). As such, the only region of NSP2 experimentally demonstrated as essential for virus replication to date is the C-terminal region (CTR) (residues 295 – 316) (**Figure 1A**) (*14–16*). We have recently demonstrated that C-terminally truncated NSP2 (NSP2-ΔC) has significantly reduced RNA annealing activity in vitro (*17*). This collectively suggests that the CTR is required for the RNA chaperone activity of NSP2, although its exact functional role(s) remained unclear.

Here, we used a single-molecule fluorescence spectroscopy approach to decouple the RNA annealing and RNA unwinding activities of full-length NSP2 and NSP2-ΔC. While NSP2-ΔC exhibits a reduced capacity to promote RNA-RNA interactions, it possesses enhanced RNA unwinding activity. To resolve these paradoxical observations, we determined cryo-EM structures of NSP2 and an NSP2-ribonucleoprotein (RNP) complex at global resolutions of 3.9 Å and 3.1 Å, respectively. In the RNP structure, the RNA density localized to surface-exposed positively-charged grooves, with no evidence of the CTR interacting with the RNA. To directly map the RNA-binding surfaces of NSP2, we employed complementary structural proteomics tools that revealed that all RNA-protein contacts required for non-specific, high-affinity RNA recognition were outside the CTR.

Furthermore, our data show that, while CTR does not directly interact with RNA, it contains a conserved acidic patch that is poised towards bound RNA. Mechanistically, we demonstrate that that the CTR promotes RNA release, indicating that the CTR is required for preventing the formation of a highly stable, kinetically trapped RNP complex that is not conducive to RNA-RNA annealing. To validate our model, we showed that alanine substitutions of the conserved acidic residues (D306, D310, E311) abrogated rotavirus replication, while charge-preserving mutations had no detrimental effect on the virus rescue in reverse genetics experiments. Our multifaceted approach provides a mechanistic basis for RNA release from high-affinity capture by NSP2, which is required for RNA annealing, chaperone dissociation, and ultimately efficient selection and packaging of a complete RV genome.

Results

Conserved NSP2 CTR is required for efficient RNA annealing

The C-terminal region (CTR) of NSP2 consists of a flexible linker (residues 295 - 304) that tethers an α-helix (C-terminal helix, CTH) to $NSP2_{core}$ (i.e. residues 1 – 294, **Figure 1A**). The CTH is ampholytic, containing highly-conserved positively- (Arg307, Lys308) and negatively-charged (Asp306, Asp310, Glu311) residues. To interrogate the role of the CTR in NSP2 function, we generated a C-terminally truncated NSP2 construct (NSP2-ΔC, residues 1 – 294) lacking the entire CTR (**Supplementary Figure S1**). This NSP2-ΔC construct has been previously characterised by others (*9*, *18*) (**Figure 1**).

To visualise the CTR conformation in solution, we determined a cryo-EM 3D reconstruction of full-length NSP2 (henceforth referred to as NSP2) at a global resolution of 3.9 Å (**Figure 1C; Supplementary Figures S2 & S3**). As expected, our cryo-EM-derived model of NSP2 was highly similar to previously solved crystal structures of NSP2 (the overall RMSD between equivalent Cα atoms of the refined model presented here and PDB 1L9V is 1.124 Å) (*7*, *9*, *18*). Within our density map, the C-terminal helix (CTH) exhibited well-resolved density (local resolutions ranging between 3.6 – 4.0 Å (**Supplementary Figure S2**)). Due to intrinsic flexibility, the linker region was poorly resolved (**Supplementary Figure S4**). We confirmed that NSP2-ΔC remains octameric by determining a negative-stain EM 3D reconstruction (**Supplementary Figure S1**).

Next, we investigated the role of CTR in the RNA annealing activity of NSP2 using a fluorescence cross-correlation (FCCS)-based RNA-RNA interaction assay (*17*). We chose RNA transcripts S6 and S11, representing rotavirus gene segments 6 and 11, as these have been previously shown to form stable RNA-RNA contacts in the presence of NSP2 (*17*). In brief, fluorescently-labelled rotavirus ssRNA genome segments (S6 and S11) were co-incubated in the absence or presence of either NSP2 or NSP2-ΔC. Ensuing intermolecular interactions were then quantitated in solution by measuring the cross-correlation function (CCF) amplitudes (**Figure 2A**). While a zero CCF amplitude is indicative of non-interacting RNAs, increasing yields of intermolecular interactions result in proportionally higher, non-zero CCF amplitudes (*19*).

Co-incubation of S6 and S11 transcripts alone results in a near zero CCF amplitude indicating that they do not spontaneously interact (**Figure 2B and Supplementary Figure S5**). In contrast, addition of NSP2 to an equimolar mixture of these two RNAs produced a high CCF amplitude, indicative of intermolecular RNA duplex formation (**Figure 2B**). This observation is in agreement with the known role of NSP2 as an RNA chaperone, facilitating the remodelling and annealing of structured RNAs (*17*).

Co-incubation of S6 and S11 in the presence of NSP2–ΔC results in a reduced CCF amplitude (**Figure 2B**), indicating that NSP2-ΔC has a reduced RNA annealing activity relative to full-length NSP2. This is in agreement with our previous observation that NSP2-ΔC has reduced capacity to promote interactions between RV segments S5 and S11 (*17*). In addition, our combined data confirms that CTR plays a role in the RNA chaperone function of NSP2 irrespective of the RNA substrates chosen.

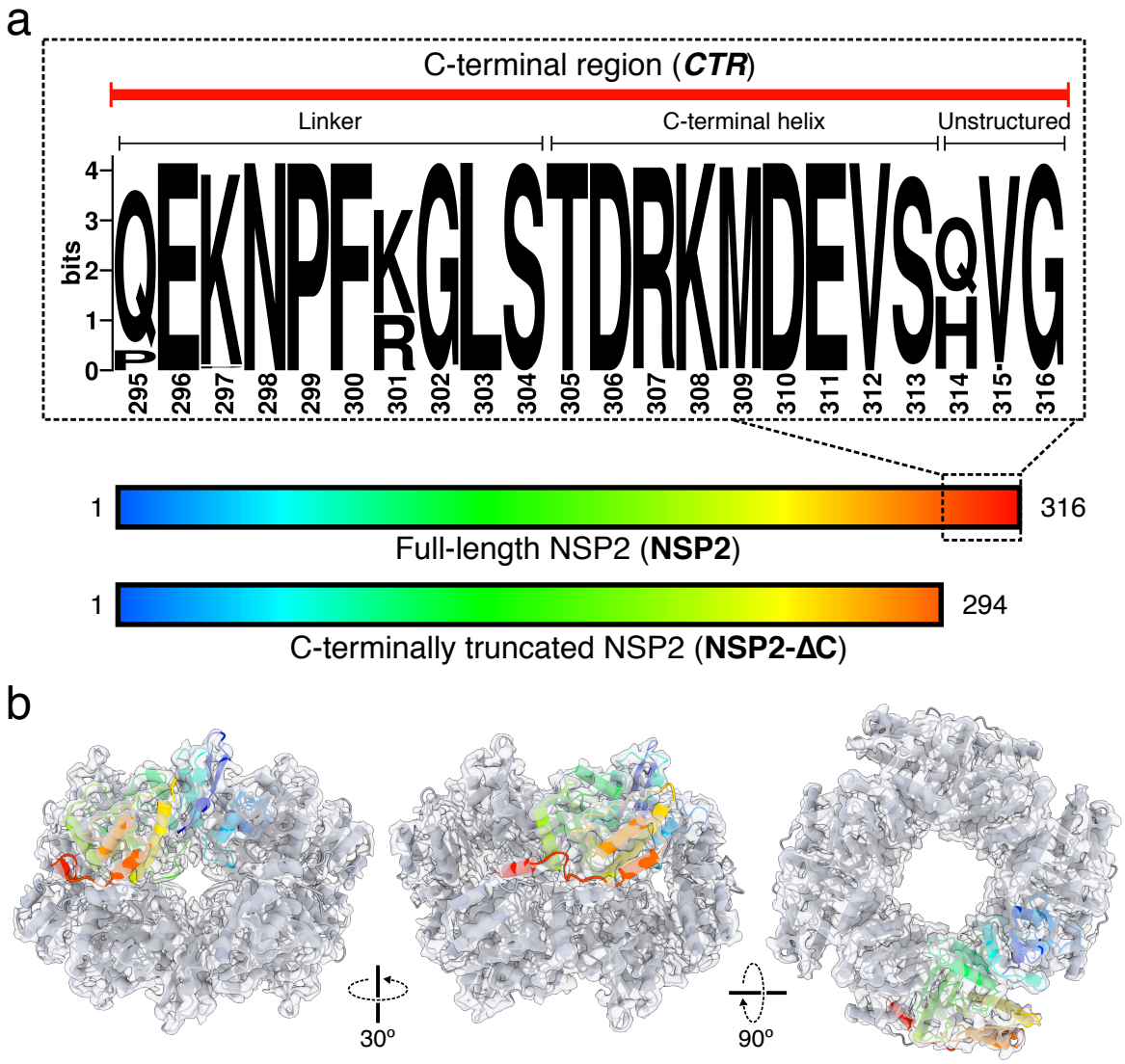

Figure 1. Structure and conservation of NSP2 CTR. A: Constructs of full-length NSP2 (NSP2) and C-terminally truncated NSP2 (NSP2-ΔC, residues 1 – 294) used in this study. An expanded, annotated sequence logo of the NSP2 CTR is shown, which consists of an unstructured, flexible linker region (residues 295 – 304) and a single alpha helix (C-terminal helix, CTH, residues 305 – 313). Downstream residues (314 – 316) are non-essential for viral replication. **B**: A 3.9 Å resolution cryo-EM reconstruction of the octameric NSP2 apoprotein (grey transparent surface) with associated model (cartoon). A single monomer is highlighted and color coded according to sequence position shown in panel A.

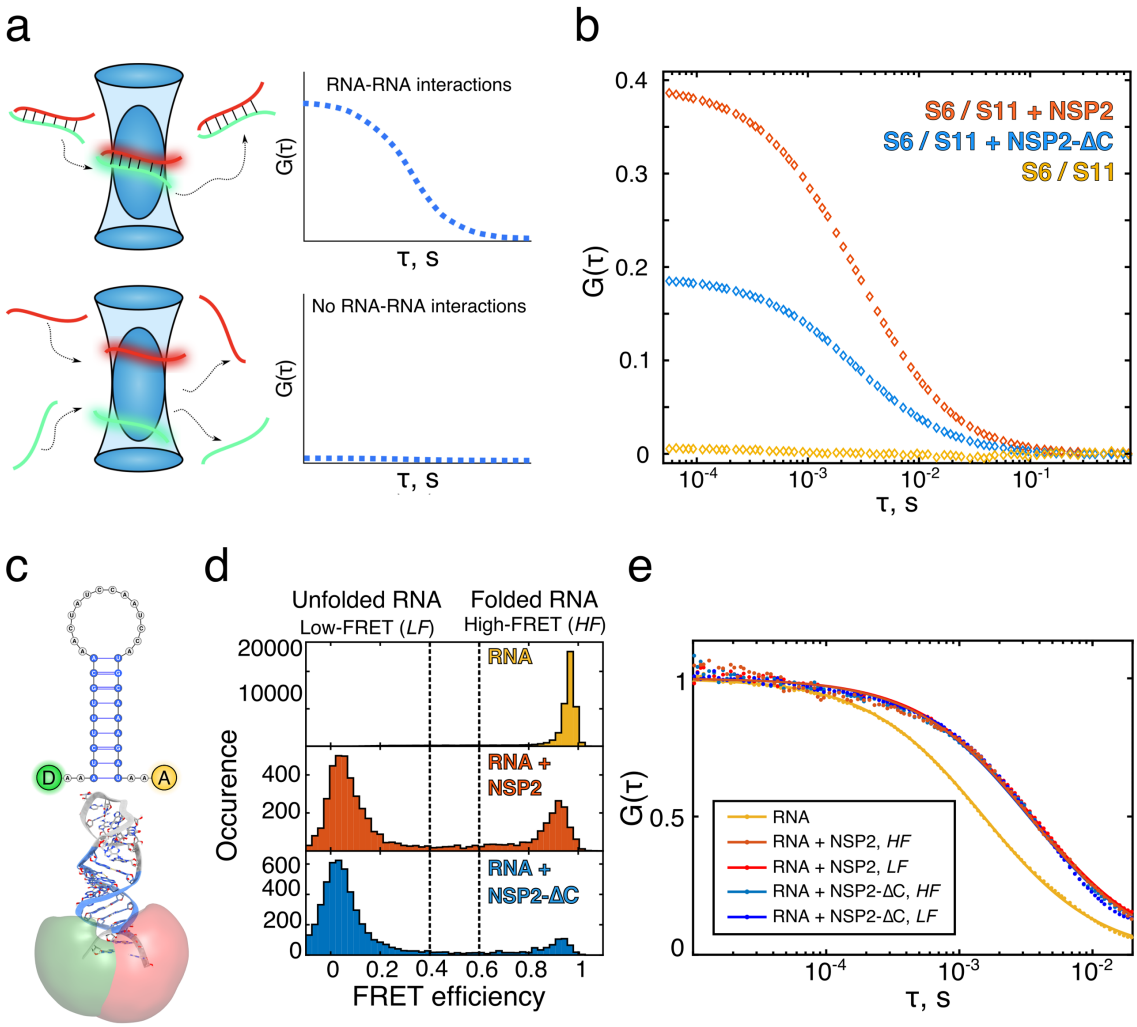

Figure 2. The NSP2 CTR is required for RNA-RNA matchmaking and RNA unwinding. A: Schematics of fluorescence cross-correlation spectroscopy (FCCS) experiment to probe RNA-RNA interactions between fluorescently labelled transcripts S6 (green) and S11 (red). Upon strand annealing, transcripts co-diffuse (shown as a duplex within the blue confocal volume). Such interactions result in a non-zero amplitude of the cross-correlation function G(τ), and thus directly report the fraction of interacting RNAs. A CCF amplitude G(τ) = 0 indicates that the two RNA molecules diffuse independently and are not interacting. **B**: Equimolar amounts of S6 and S11 were co-incubated in the absence (yellow) or presence of either NSP2 (orange) or NSP2-ΔC (blue). While S6 and S11 do not spontaneously interact, co-incubation with NSP2 results in a high fraction of stable S6:S11 complexes. In contrast, co-incubation of S6 and S11 with NSP2-ΔC results in 2-fold reduction of the fraction of S6:S11 complexes. **C**: The RNA stem-loop construct used in the smFRET studies of RNA unwinding activity. The FRET donor (D, green) and acceptor (A, red) dye reporters (Atto532 and Atto647N) and their calculated overlapping accessible volumes (green and red, respectively) are shown. **D**: smFRET efficiency histograms of the RNA stem-loop alone (top, yellow) and in the presence of 5 nM NSP2 (middle, red) or 5 nM NSP2-ΔC (bottom, blue). **E**: A species-selective correlation analysis was performed on the high FRET (*HF*) and low FRET (*LF*) species of RNA stem-loops bound to NSP2 (in orange) and NSP2-ΔC (in blue). For comparison, we also did a species FCS analysis of the free RNA data. All FCS analyses were performed on the smFRET data shown in panel D.

The NSP2 CTR reduces the RNA unwinding activity but does not directly interact with RNA

As the ability of NSP2 to unfold and remodel RNA structures is a prerequisite for its RNA annealing activity (*4*), we next investigated the role of the CTR in RNA helix destabilisation. We used single-molecule Förster Resonance Energy Transfer (smFRET) to directly compare the abilities of NSP2 and NSP2-ΔC to unwind an RNA stem-loop labelled at the 5' and 3' termini with donor and acceptor dyes (Atto532 and Atto647N) (**Figure 2C**).

In the absence of either protein, the stem-loop alone adopts a folded conformation, resulting in a single, high-FRET population (E_{FRET} = ~0.95) (**Figure 2D**). Incubation with NSP2 produces two distinct FRET populations, corresponding to fully folded d(E_{FRET} = ~0.95) and unfolded (E_{FRET} = ~0.05) RNA states. No intermediate FRET populations (corresponding to partially-unwound stem-loop conformations) were observed, in agreement with previous observations of NSP2-mediated RNA unwinding (*4*).

We then measured the ability of NSP2-ΔC to unwind this RNA stem loop. Surprisingly, in the presence of NSP2-ΔC, the stem-loop was predominantly unfolded (E_{FRET} = ~0.05) (**Figure 2D**). Furthermore, we did not observe differences in binding of either NSP2 or NSP2-ΔC to both folded and unfolded RNA conformations (**Figure 2E**). These data demonstrate that NSP2-ΔC has enhanced RNA unfolding activity compared to its full-length counterpart. This result is somewhat paradoxical: while NSP2-ΔC is more efficient at destabilizing RNA structure (**Figure 2D**), it is approximately half as efficient at promoting the annealing of structured RNAs as NSP2 (**Figure 2B**).

To deduce whether the CTR directly interacts with RNA, we used a combination of structural proteomics techniques (**Figure 3**). We performed hydrogen-deuterium exchange-mass spectrometry (HDX-MS) experiments to map regions of NSP2 that become protected from deuterium exchange in the presence of RNA, presumably as they are involved in RNA binding and occluded from solvent when bound. We observed significant protection from exchange for peptides that predominantly mapped to ~25 Å-deep grooves present on the surface of NSP2, indicating that this is the major RNA-binding site of NSP2 (**Figure 3A**). Intriguingly, we did not observe any significant change in protection for peptides that spanned the CTR, indicating that the CTR does not directly interact with RNA (**Figures 3A & 3B), Supplementary Figure S7**).

We further corroborated the location of RNA-binding sites on NSP2 using UV-crosslinking with RBDmap (*20*, *21*). Consistent with the HDX-MS data, RBDmap identified RNA-linked peptides map to these surface-exposed RNA-binding grooves (**Figure 3C & 3D, Supplementary Figure S7**). However, we again did not observe any RNA-linked peptides corresponding to the CTR.

Collectively, these results reinforce the notion that the CTR is involved in the RNA chaperone activities of NSP2. Our data indicates that although the CTR does not directly interact with RNA, it is a determinant of both the RNA unwinding and annealing activities of NSP2.

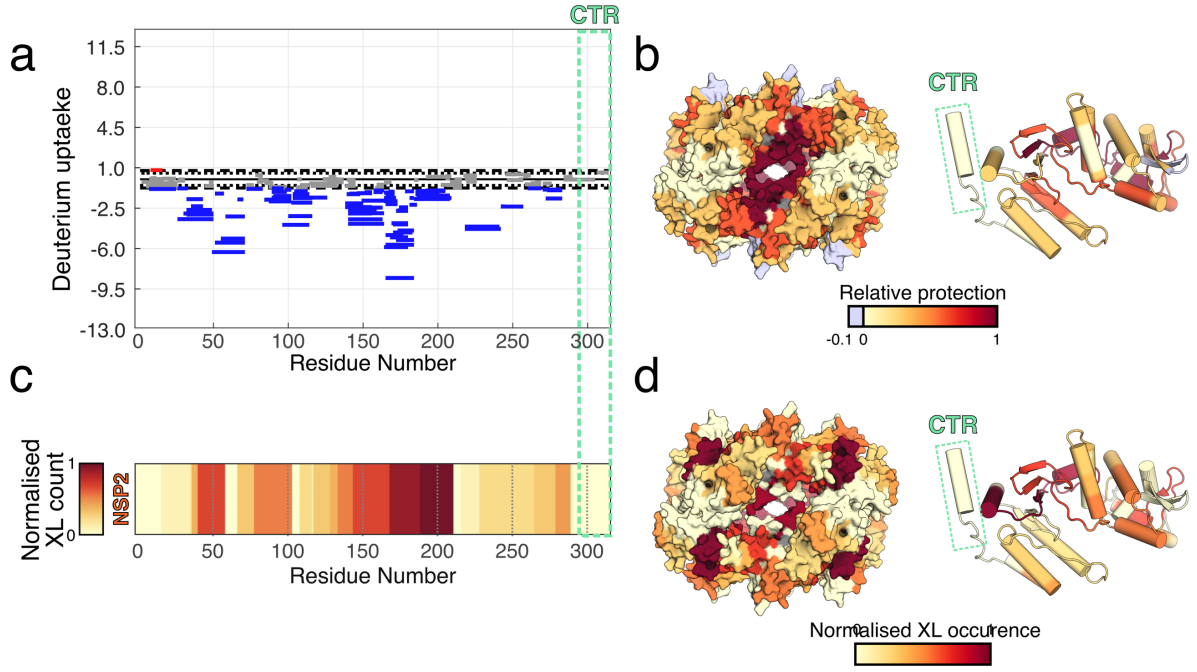

Figure 3. The CTR does not interact with RNA. A: Wood's plots showing summed differences in deuterium uptake in NSP2 over all four different HDX timepoints, comparing NSP2 alone with NSP2 in the presence of RNA. Protected and deprotected peptides are colored blue and red, respectively. Peptides with no significant difference between conditions, determined using a 99% confidence interval (dotted line), are shown in grey. Green dashed box corresponds to the CTR, showing no significant difference in exchange in the presence or absence of RNA. **B**: A differential hydrogen-deuterium exchange (HDX) map colored onto the NSP2 octamer surface (left) and monomer structure (right). Multiple regions of the NSP2 are protected in the presence RNA. Note that, upon RNA binding, the protection rates of the CTR (green box) are not changed. **C**: Normalised occurrence of RNA-interacting peptides determined using UV crosslinking (identified by RBDmap) as a function of sequence position of NSP2. Green box denotes CTR. **D**: RBDmap-identified RNA-binding peptides mapped mapped onto the surface of NSP2 octamer (left) and its monomer (right). Structures are colored according to frequency of crosslink occurrence. No RNA:peptide cross-links are mapped onto the CTR (green box).

Cryo-EM visualization of NSP2-RNA interactions

To understand the molecular basis for the RNA binding by NSP2, we determined a cryo-EM reconstruction of an NSP2 ribonucleoprotein (RNP) complex at a global resolution of 3.1 Å (**Figure 4A, Supplementary Figure S8**). While the cryo-EM density corresponding to NSP2 was well resolved, there was no density that could be attributed to the RNA in the high-resolution post-processed NSP2-RNP map (**Figure 4A**). This is likely due to the heterogeneity and intrinsic flexibility of the NSP2-bound unstructured single-stranded RNA. Despite this, a novel feature localised to RNA binding sites identified by HDX-MS and RBDmap (**Figure 3**) was present in 5 Å low-pass filtered (LPF) maps (**Figure 4B**). Notably, such a density feature was not present in 5 Å-LPF NSP2 apoprotein maps (**Figure 4C**). We therefore attribute this density to NSP2-bound RNA.

To improve visualization of the RNA density, we performed focused classification using C4 symmetry-expanded data with a mask applied to a single RNA-binding face of NSP2 (*22–24*). The resulting 3D reconstructions readily classified into four dominant populations, three of which had poor RNA occupancy (each class with 26% of the input particles), while a single 3D class average (22% of input particles) exhibited improved RNA density (**Supplementary Figure S8**). Due to the reasons outlined above, the diffuse nature of this density prevented us from modelling the ssRNA into the structure. However, we were able to visualise residue-specific NSP2-RNA contacts (**Figure 4D**).

We built an atomic model of NSP2 into the sharpened map and then computed a difference map between NSP2 and the RNA-occupied, focused map in order to visualise the NSP2-RNA contacts. Significant positive density was localised in the basic groove of NSP2 (**Figure 4**), consistent with the binding site identified through HDX and RBDmap (**Figure 3**). We observed interactions between positively-charged residues, most notably Arg68 (**Figure 4D**). Adjacent to this contact are Lys58, Lys59, and Arg60, of which Lys59 and Arg60 are directly oriented towards the RNA density (**Figure 4D**, inset). The importance of these residues for RNA capture by NSP2 is strongly supported by previous biochemical studies that identified a number of solvent-exposed lysine and arginine residues (Lys37, Lys38, Lys58, Lys59, Arg60, Arg68) that span the periphery of the NSP2 octamer (**Supplementary Figure S9**) and contribute to RNA binding (*25*).

Furthermore, the identified residues are localised to an unstructured loop within the RNA-binding groove, allowing promiscuous and flexible accommodation of alternative RNA structures with near-identical affinities by NSP2, consistent with previous reports (*4*, *26*). Together with our HDX and RBDmap results, our cryo-EM reconstruction reveals a number of electrostatic contacts that provide a plausible molecular basis for non-specific NSP2-RNA interactions (**Figure 4D**, inset). In addition, our EM reconstruction has revealed a number of other residues (Arg240, Lys286, Phe290) that likely contribute to RNA binding, also identified by HDX and RBDmap (**Supplementary Figures S7 & S9**). These residues may also participate in non-specific RNA contacts via electrostatic interactions, hydrogen bonding and π-π stacking, consistent with a significant non-electrostatic contribution to the overall free energy of RNA binding to NSP2.

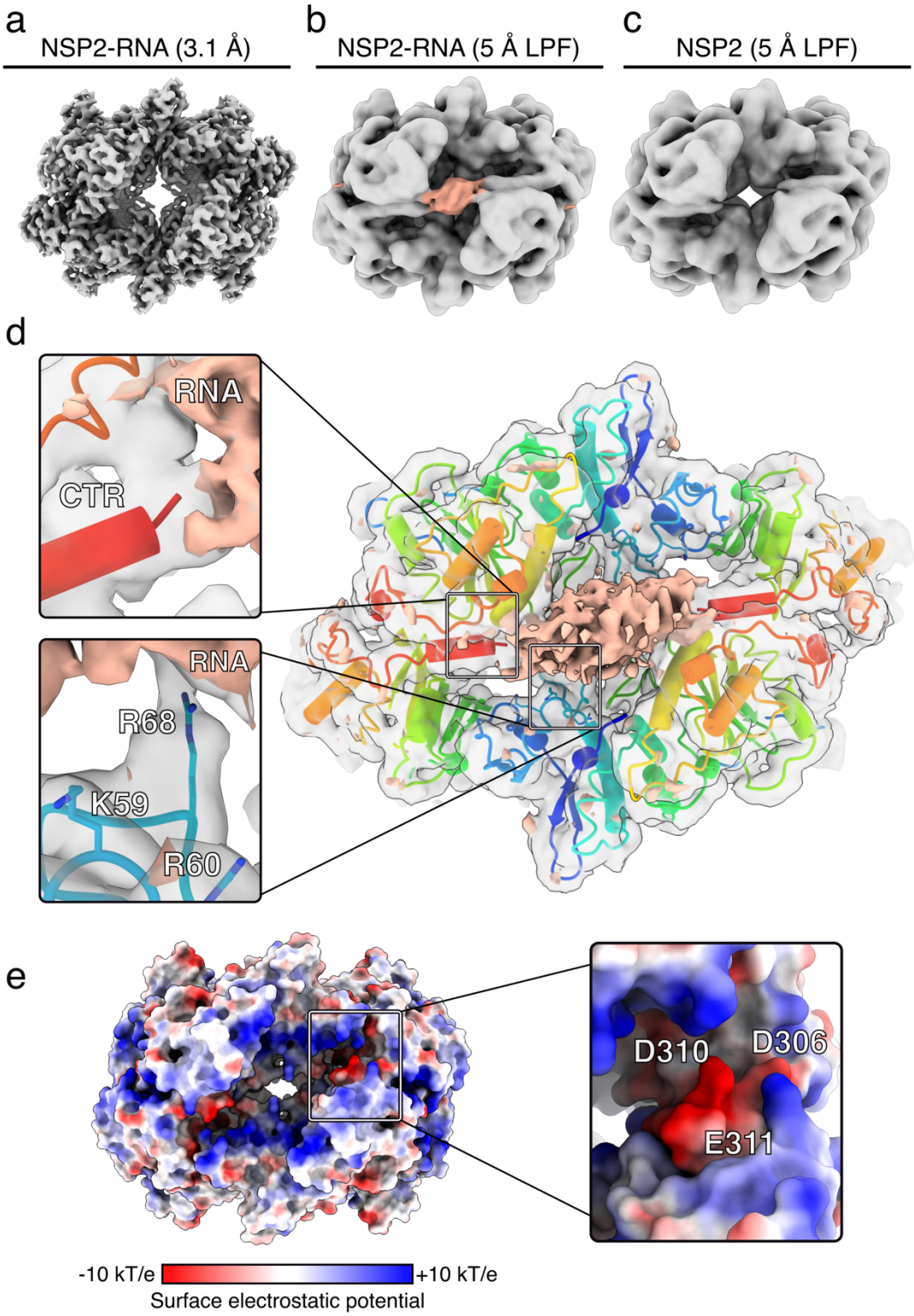

Figure 4. Cryo-EM structure of the NSP2-RNP complex. A: 3.1 Å-resolution reconstruction of the NSP2-RNP complex **B & C**: NSP2-RNP (B) and NSP2 apoprotein (C) cryo-EM maps low-pass filtered (LPF) to 5 Å. A novel cryo-EM density feature attributed to RNA (peach) in the LPF RNP map (B) is highlighted by the dashed box. Both maps are reconstructed with D4 symmetry. **D**: Direct visualisation of interactions between NSP2 and RNA using C4 symmetry expansion and focused classification. The positive difference density map corresponding to

RNA (peach) is overlaid onto the unsharpened NSP2-RNP complex map determined through symmetry expansion and focused classification (grey, transparent density) and atomic model of NSP2. Inset: zoom in of CTR positioned relative to RNA density (top) and RNA-interacting residues (bottom). **E**: The surface electrostatic potential analysis of NSP2 surface is shown (blue is positively-charged; red is negatively-charged). Inset: zoom in of CTR, with residues forming acidic patch (D306, D310, E311) annotated.

Conserved acidic patch within the CTR promotes RNA dissociation

Within the cryo-EM density map, the CTRs are poised below the RNA, while making limited contacts with the observed RNA density (**Figure 4D**). This suggests that rather than modulating the RNA binding affinity, the CTR may play a role in promoting RNA dissociation from NSP2. To investigate this, we performed binding kinetics measurements using surface plasmon resonance (SPR) (**Figure 5A & B**). Association rate constants (K_{on}) remain largely consistent across a range of concentrations of both NSP2 and NSP2-ΔC (NSP2-ΔC binds 1.5 ± 0.4-fold faster than NSP2 **Table 3**). However, NSP2-ΔC exhibited 3.2 ± 0.3-fold slower dissociation than NSP2, suggesting a role for CTR in the displacement of bound RNA (**Figure 5A**, **Table 3**).

Close examination of our cryo-EM-derived model revealed an acidic patch within the CTR, (**Figure 4E & F**). This is in contrast to other clusters of surface-exposed acidic residues on NSP2 that show a low degree of conservation (**Supplementary figure S10**). The acidic patch of the CTR is presented directly underneath the density attributed to bound RNA (**Figure 4D**), potentially promoting RNA displacement from the NSP2. Such displacement could be achieved either via direct competition with RNA-binding residues or by providing a negatively-charged environment that accelerates RNA dissociation from NSP2 through charge repulsion.

Therefore, to further investigate RNA displacement from NSP2, we used RNA competition assays (**Figure 5C & D**). We performed titrations of unlabelled RNA into preformed RNP complexes containing fluorescently-labelled RNA to understand the differences in RNA exchange and chaperone recycling between NSP2 and NSP2-ΔC. Using fluorescence anisotropy, we estimated the degree of competition as the concentration of competitor RNA required to displace 50% of pre-bound RNA from either NSP2 or NSP2-ΔC complexes (IC_{50}). We determined IC_{50} values of 208 ± 11 nM and 890 ± 160 nM for NSP2 and NSP2-ΔC, respectively, confirming that NSP2–ΔC undergoes ~4-fold reduced RNA exchange, consistent with its ~3-fold slower rate of dissociation from RNA (**Figures 5A & B**).

We then investigated whether the CTR promotes RNA dissociation from NSP2 through directly competing with RNA for binding to basic, RNA-binding residues on the $NSP2_{core}$. To achieve this, we measured RNA binding by NSP2-ΔC in the presence of saturating amounts of a synthetic peptide matching the sequence of the CTR. No dissociation of RNA from the NSP2-ΔC was observed in the presence of 20-fold molar excess of the CTR peptide over NSP2-ΔC (**Figure 5D**). Furthermore, no RNA binding was observed upon incubation with 10 μM CTR peptide (i.e. 400-fold excess), indicating that the CTR does not bind RNA. This suggests that, while the CTR is required for RNA displacement from NSP2, this does not occur through direct competition.

We analysed our atomic model of NSP2 to evaluate the distances between acidic residues within the CTR and the basic, RNA-binding residues localised to flexible loops within the RNA-binding grooves (**Figure 5E, Supplementary Figure S11**). The distances (~10 – 30 Å) between acidic residues within the CTR and the RNA-interacting residues are incongruent with a direct competition model. While R68 was demonstrated to directly interact with RNA (**Figure 4D**), it is 18 Å away from acidic residues within the CTR. This further demonstrates

112 that, while CTR promotes dissociation of RNA from NSP2, it does not do so through direct
113 competition for $NSP2_{core}$ binding (**Figure 5E**). Collectively, our data suggest that conserved
114 acidic patches within the CTR promote dissociation of bound RNA from NSP2 via charge
115 repulsion.

116 Finally, to validate our findings *in vivo*, we employed a reverse genetics approach to rescue
117 recombinant rotaviruses with point mutations within the CTR. We assessed the effects of
118 amino acid substitutions within the CTR on viral replication by attempting recombinant virus
119 rescue, as described in Materials and Methods. All attempts to rescue a triple alanine mutant
120 D306A/D310A/E311A were unsuccessful, suggesting these mutations completely abrogate
121 virus replication. Remarkably, a triple mutant containing charge-preserving mutations
122 D306E/D310E/E311D was successfully rescued with the same efficiencies as wild-type virus
123 (**Supplementary Figure S13**). This directly demonstrates the essential role of the CTR acidic
124 patch in rotavirus replication.

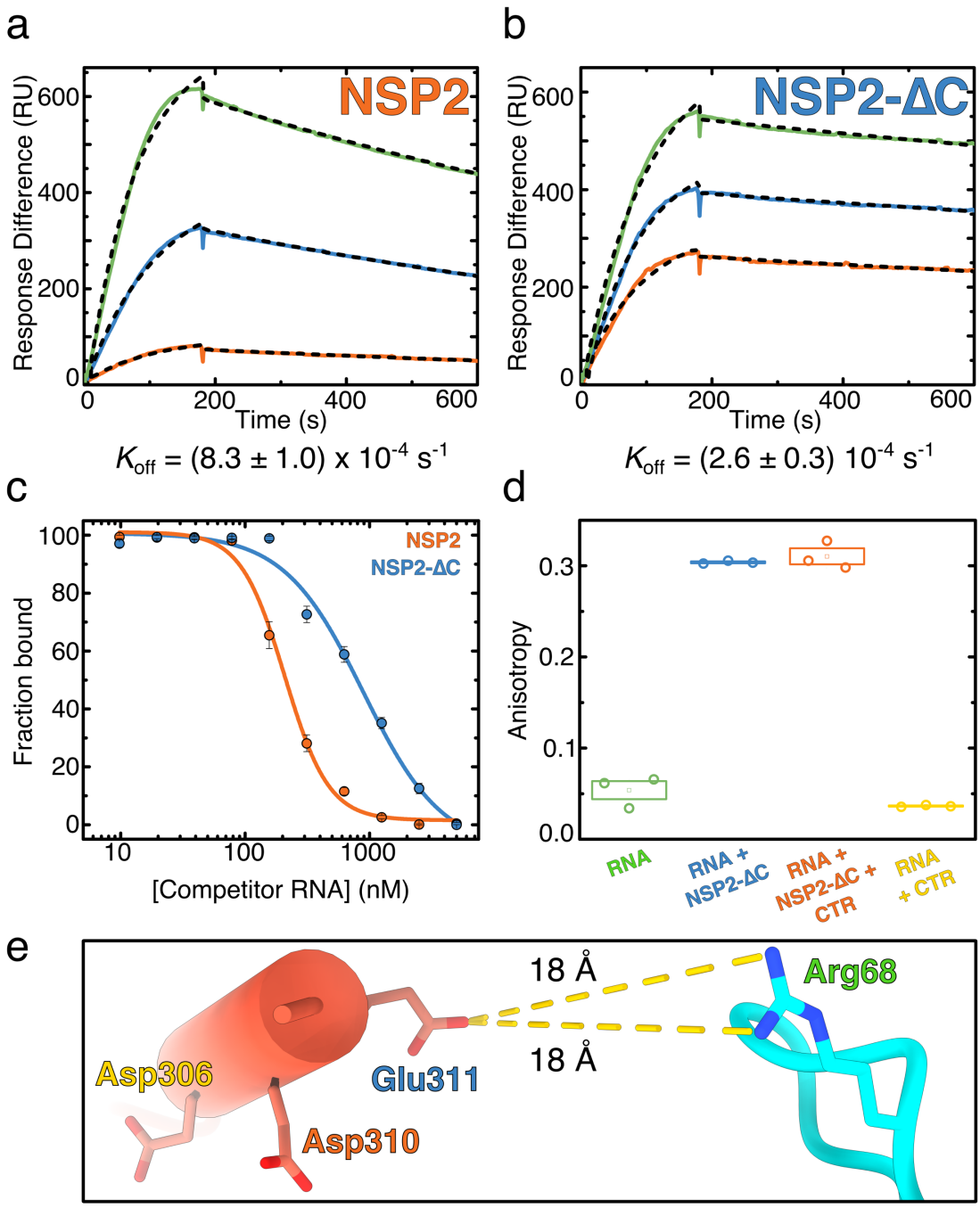

Figure 5. The CTR promotes RNA dissociation non-competitively. A & B: SPR sensograms of NSP2 (A) and NSP2-ΔC (B) binding to RNA. Although NSP2-ΔC binds RNA with ~6-fold higher affinity, this is due to a modest (1.5-fold) increase in K_{on}, and a larger (3.2-fold) decrease in K_{off}. **C**: RNA competition assay. The fractional binding of fluorescently labelled RNA was determined using fluorescence anisotropy. Labelled RNA (10 nM) fully bound to NSP2 (orange) or NSP2-ΔC (blue) was titrated with unlabelled RNA of identical sequence to compete for NSP2 binding against labelled RNA. The IC_{50} values for NSP2 and NSP2-ΔC were 208 ± 11 nM and 890 ± 160 nM, respectively. The NSP2-RNA complex undergoes strand exchange more readily than the NSP2-ΔC:RNA complex. **D**: We used fluorescence anisotropy experiments to investigate RNA binding to NSP2. Ten μM CTR peptide was added to preformed NSP2-ΔC:RNA complexes. The added CTR peptide did not

137 displace the bound RNA. Hence, a peptide corresponding to the NSP2 CTR does not compete
138 with RNA for binding to NSP2-ΔC. **E**: Distances between acidic residues within CTR and
139 R68 interacting with RNA. Note the nearest side chain of E311 which is 18Å away
140 from R68.

Discussion

Long RNAs adopt an ensemble of diverse stable structures that limit spontaneous RNA-RNA interactions through the sequestration of sequences required for intermolecular base pairing (*17*, *27–30*). This necessitates the action of RNA chaperone proteins to bind and refold RNA structures in order to promote RNA annealing between complementary sequences (*31–33*).

In order to function as an RNA chaperone, NSP2 must capture, unwind, anneal and release complementary RNA sequences (*17*, *34*, *35*). Previous structural studies have provided static snapshots of crystallographically-averaged NSP2-RNA complexes (*7*, *18*, *25*). However, due to the highly dynamic nature of the protein-RNA interactions required for its RNA chaperone activity, they have only revealed limited insights into the molecular mechanisms of NSP2. Our recent work (13, 17, 18) indicates that for NSP2-RNP complexes such heterogeneity arises from poorly defined protein-RNA stoichiometries and the ability of bound RNA to adopt multiple configurations and orientations. To overcome these challenges, here we used a combination of single molecule fluorescence, cryo-EM, structural proteomics and biophysical assays to decipher the mechanism of NSP2 chaperone function.

Previous work suggests that the C-terminal region of NSP2 is essential for rotavirus replication (*15*). Using single molecule fluorescence assays, here we have shown that the CTR of NSP2 is important for promoting RNA-RNA interactions. However, we only identified interactions between RNA and basic residues located in flexible loops within the RNA binding groove of NSP2, but not the CTR. Similar RNA recognition mechanisms have been reported in other RNA chaperones including *E. coli* StpA and HIV-1 NC (*37*, *38*). Collectively, these results highlight the role of the CTR in NSP2 RNA chaperone activity but not RNA binding.

Mechanism of the CTR-assisted RNA displacement and its role in RNA matchmaking

FCS analysis of high- and low-FRET RNA species confirms that full length NSP2 binds to both the unfolded and folded RNA conformations, priming RNAs for efficient RNA annealing (**Figure 3E, Supplementary Figure S6**). Single molecule fluorescence and binding kinetics experiments indicate that removal of the CTR does not perturb RNA binding but slows RNA release (~3.2-fold increase in k_{off}). Moreover, CTR removal results in a ~2.4-fold increase in the RNA-unwinding activity of NSP2-ΔC, as well as a ~2-fold decrease in its RNA annealing activity. Additionally, smFRET data reveal that binding to NSP2-ΔC energetically favours low-FRET (unfolded) RNA conformations, resulting in remodelling of structured RNAs (**Figure 3D**). The resulting increased stability of NSP2-ΔC-RNA complexes precludes efficient RNA annealing, yielding kinetically trapped RNP complex intermediates.

Combined, our data strongly supports a model whereby rotavirus NSP2 binds to RNA with high affinity, resulting in RNA structure destabilisation (**Figure 6A**). By binding to multiple RNAs concurrently via surface-exposed grooves (**Figure 6A, cyan**) (*4*, *7*, *17*), it acts as a matchmaker of complementary sequences, promoting intermolecular RNA-RNA interactions. Conserved acidic patches within the ampholytic CTR (**Figure 6A**, red) accelerate RNA displacement from NSP2 via charge repulsion, thus enabling RNA chaperone recycling and duplex release. Removal of the ampholytic CTRs in the NSP2 variants derived from two distinct rotavirus strains (SA11 and RF, **Supplementary Figure S12**) has a similar outcome on RNA chaperone activity *in vitro* (**Supplementary Figure S5**), suggesting a conserved role of the CTR in NSP2 function. This model is further supported by our observation that removal of the unstructured region downstream of the ampholytic CTR (**Figure 1A**) does not alter the RNA unwinding activity of NSP2 (**Supplementary Figure S6**). Interestingly, this partial truncation has been previously shown to support viral replication (*9*). Excitingly, we have exploited recent technical advances in reverse genetics of rotaviruses to directly demonstrate

189 the pivotal role of these conserved acidic residues in rotavirus replication (**Supplementary**
190 **Figure S13**).

191 The described principle of CTR-assisted RNA dissociation from NSP2 is strikingly similar to
192 that of the bacterial RNA chaperone protein Hfq (*39–41*). Hfq possesses an unstructured C-
193 terminal domain (CTD) with an acidic tip that drives RNA displacement from the Hfq_{core} (*42*).
194 Unlike the Hfq CTD, we do not observe competition between CTR and RNA for $NSP2_{core}$
195 binding (*43*, *44*). Nevertheless, the NSP2 CTR modulates the kinetics and thermodynamics of
196 NSP2-RNP complex formation to accomplish RNA chaperone recycling. This may represent
197 a conserved mechanistic feature of multimeric RNA chaperones that capture RNA with high
198 affinity and require auto-regulation to assist RNA dissociation in order to promote efficient
199 matchmaking.

200

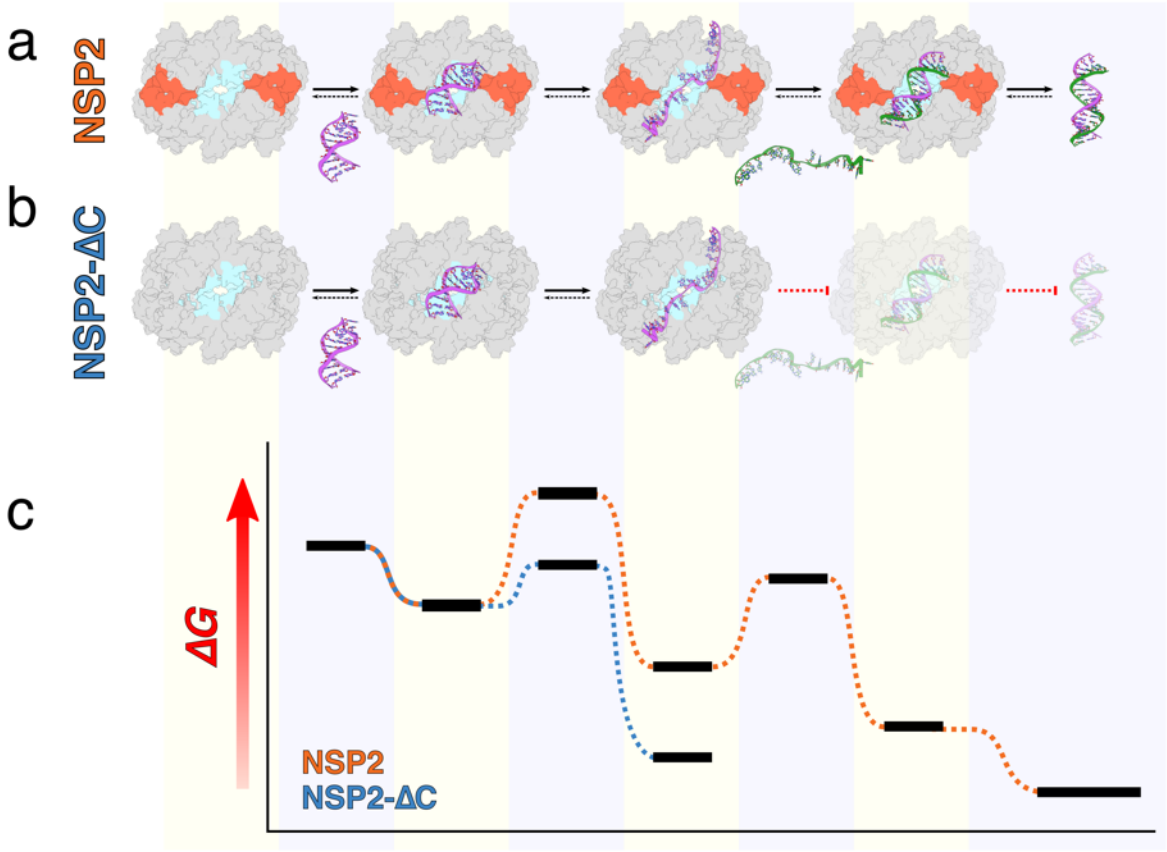

Figure 6. Proposed mechanism of CTR-accelerated RNA dissociation and its requirement for efficient NSP2-mediated RNA-RNA interactions. A: NSP2 captures RNA (purple) via a positively-charged groove (cyan) and promotes RNA unwinding. Binding of a second, complementary RNA strand (green) by NSP2 allows efficient annealing and the proximity to the CTR (burnt orange) promotes dissociation of dsRNA from the NSP2. **B**: In contrast, NSP2-ΔC captures and unwinds RNA, forming a highly stable intermediate. The stability of the intermediate state makes displacement of the bound RNA by a complementary RNA segment via annealing thermodynamically unfavourable. **C**: A free energy diagram of NSP2 (orange) and NSP2-ΔC (blue)-mediated RNA annealing. Horizontal black bars correspond to the free energy levels of different RNA states corresponding to the above schematic representations in A & B.

Materials and Methods

Protein and RNA production

NSP2 and NSP2-ΔC (RVA strains SA11 and RF) were expressed and purified as described previously (*17*). RNAs used in this study are listed in **Supplementary Table S1**. RNA sequences S5, S6 and S11 were produced and labelled using previously-described *in vitro* transcription and labelling protocols (*17*). Unstructured 20mers (labelled and unlabelled), unstructured 10mer (labelled) and biotinylated unstructured 10mer RNAs were purchased from Integrated DNA technologies (IDT). Dual-labelled stem loop RNA was purchased from IBA Life Sciences.

Negative stain electron microscopy and data processing

For negative-stain grid preparation, 4 μl of sample (at various concentrations ranging from 100 – 500 nM) was incubated on glow-discharged (using PELCO easiGlow) carbon-coated Formvar 300-mesh Cu grid (Agar scientific) for 90 seconds prior to blotting, and stained twice with 20 μl 2% uranyl acetate (first stain immediately blotted, the second stain incubated for 20 seconds prior to blotting) and allowed to dry. Micrographs were collected on a FEI Tecnai 12 transmission electron microscope operated at 120 kV and equipped with a Gatan UltraScan 4000 CCD camera operated at a nominal magnification of 30,000 x (giving a 3.74 Å / pixel sampling on the object level). From 23 micrograph images taken with a nominal defocus of -3 μm, 14,740 particles were picked using template-based autopicking within Relion 3. Multiple rounds of 2D and 3D classification resulted in the selection of a subset of 2,864 particles. These particles were used to determine a ~22 Å resolution NSP2-ΔC reconstruction with D4 symmetry applied.

Cryogenic electron microscopy (cryo-EM) and data processing

Cryo-EM was performed exclusively with Quantifoil R.1.2/1.3 holey carbon grids (i.e. regular ~1.2 μm circular holes with a regular spacing of ~1.3 μm), purchased from Quantifoil. All grids were glow discharged in air using GloQube glow discharge system (Quorum) immediately prior to use. All grids were prepared using a Vitribot IV (FEI) at 100% humidity and 4°C, with a blotting time of 6 seconds and a nominal blotting force of 6. Samples were flash-frozen in liquid nitrogen (LN_2)-cooled liquid ethane and immediately transferred to storage dewars under LN_2.

Vitrified samples were imaged at low temperature in-house (Astbury Biostructure Laboratory, University of Leeds), using Thermo Fisher Titan Krios microscopes equipped with either a Falcon III (NSP2 apoprotein) or a Gatan K2 (NSP2-RNP) detector. Data was collected with an acceleration voltage of 300 kV and a nominal magnification of 75,000x, resulting in pixel sizes of 1.065 Å (Falcon III) or 1.07 Å (K2). Data collection parameters are described in **Supplementary Table 2**.

Image processing was carried out using the Relion 3 pipeline (*45*). Movie drift-correction was performed using MOTIONCOR2 (*46*), and the contrast transfer function of each movie was determined using gCTF (*47*). Initial particle autopicking of a subset of 5 – 10 randomly chosen micrographs was performed with the Laplacian-of-Gaussian (LoG) tool within the Autopicking module of Relion3. Particles were extracted and subjected to initial 2D classification in order to identify particles and assess autopicking success. Following this, the entire dataset was picked using LoG methods, extracted using 256 pixel box size and binned four times (effective box size 64 pixels) and subjected to 2D classification with fast subsets in order to remove false-positive particles that had been erroneously picked. Next, a more rigorous 2D classification was performed (without fast subsets). Particles originating from 2D classes with secondary structural features were selected and used to generate an initial model. Following

262 multiple rounds of 3D and 2D classification, suitable particles were selected for 3D auto-
263 refinement and various symmetry parameters were applied. Following refinement, per-particle
264 CTF and Bayesian Polishing were performed in Relion 3, and 'shiny' particles were re-refined.
265 Post-processing was performed with a soft mask of 15 pixels and the B-factor estimated
266 automatically in Relion 3.

267 After particle polishing, the NSP2 apoprotein and the NSP2-RNP complex were subjected to
268 further 3D classification into three classes without particle orientations. This yielded three
269 similarly-sized subsets of near-identical particles for the NSP2 apoprotein whose resolution
270 did not improve upon the original, larger dataset following 3D auto-refinement and post-
271 processing. For the NSP2-RNP complex, this gave a single class with 86% of particles, and
272 two other classes with 6% and 8% of the particles. The class with 6% of input particles had
273 well-defined protein and RNA densities and was used for 3D auto-refinement and post-
274 processing. This improved the map resolution from 3.5 Å to 3.4 Å with C4 symmetry. A D4
275 symmetry reconstruction further increased the map resolution from 3.5 Å to 3.1 Å.

276 For the NSP2 RNP complex, symmetry expansion was performed on a subset of the 635,599
277 particles used for a C4 symmetry reconstruction using the *relion_particle_symmetry_expand*
278 command, generating four symmetry-related orientations for each particle. A mask covering
279 a single basic groove-face of NSP2 was made using the volume eraser tool in UCSF
280 ChimeraX (*48*) and Relion 3, with a soft edge of 15 pixels (**Supplementary Figure S8**). The
281 symmetry-expanded dataset was then subjected to focussed classification into 10 classes
282 using this mask without particle orientations. Suitable classes (four classes containing >99%
283 of input particles) were selected, and manually examined for putative RNA density. The subset
284 of particles with the strongest RNA density feature were reconstructed without a mask, and
285 subjected to masking (with the mask corresponding to the entire NSP2 octamer rather than a
286 single face) and post-processing as described for reconstructions with D4 symmetry imposed.
287 Sharpened asymmetric and D4 symmetry maps were aligned using the Fit-In-Map tool within
288 UCSF Chimera and had a correlation of 0.9663.

289 **Atomic model building**

290 A previous atomic model of NSP2 (PDB 1L9V) was fit into the cryo-EM densities using
291 ChimeraX (*48*), and subjected to automated flexible fitting and refinement using Namdinator
292 (*49*). The Namdinator model was used for multiple iterative rounds of manual adjustment in
293 Coot (*50*) and real-space refinement in Phenix (*51*). Models for NSP2 apoprotein and NSP2-
294 RNP were validated using MolProbity (*52*) as implemented in Phenix.

295 **Protein Sequence Conservation Analysis**

296 Full-length NSP2-coding sequences of group A rotaviruses were obtained from GenBank.
297 Sequences of avian strains and of rearranged RNA segments of mammalian strains were
298 excluded from the analysis. Protein sequence conservation and multiple sequence alignment
299 (MSA) was performed using the online ConSurf (*53*) server. Output from the ConSurf MSA
300 was used to generate a sequence logo using the WebLogo server (*54*). Maps and models
301 were visualized using ChimeraX (*48*) and the electrostatic surfaces were determined using
302 the APBS plugin (*55*).
303
304 **Single-molecule (sm)FRET measurements**

305 SmFRET measurements of freely diffusing dual-labeled RNA stem-loops in the presence and
306 absence of NSP2 were performed on a home-built confocal microscope as described
307 previously (*4*). Briefly, the samples were excited using pulsed interleaved excitation (*56*) at
308 wavelengths of 532 and 640 nm (PicoTA, Toptica and LDH-D-C-640, PicoQuant) with typical
309 laser powers of 100 μW as measured before the 60x water immersion objective (Plan Apo IR

310 60x/ 1.27 WI Nikon, Düsseldorf, Germany). The fluorescence signal was split between the
311 green and red detection channels using a DualLine Z532/635 beamsplitter (AHF) and the
312 emission spectra filtered using a Brightline 582/75 filters (Semrock) for green detection and
313 HQ700/75 and ET700/75 filters (Chroma) for red detection. Measurements were performed in
314 eight-well chamber slides (Nunc Lab-Tek, VWR) in a buffer composed of 1/3 PBS (45 mM
315 NaCl, 3 mM phosphate, 1 mM KCl), 1 mM Trolox to reduce photobleaching (*57*) and 0.01%
316 (v/v) Tween20 to prevent sticking of the sample to the glass surface. The dual-labeled RNA
317 stem-loop was diluted to 25 pM and incubated with 5 nM NSP2 (either full length or the ΔC
318 mutant). Data were analyzed with the open-source software package PAM (*58*) using the
319 same burst search parameters and correction factors as described in (*4*). To determine
320 species-selective fluorescence correlation functions, we defined two sub-populations based
321 on the FRET efficiency E: the low-FRET population with $E < 0.4$ and the high-FRET population
322 with $E > 0.6$. For each burst, the correlation function for acceptor photons after acceptor
323 excitation was calculated including photons within a time window of 20 ms.

324 **Surface plasmon resonance (SPR)**

325 A Biacore 3000 was used to analyse the binding kinetics of NSP2 and NSP2-ΔC to
326 5'biotinylated-10mer RNA (**Supplementary Table S1**). All experiments were performed in
327 SPR buffer (150 mM NaCl, 25 mM HEPES, pH 7.5, 0.1 % Tween-20). RNAs were immobilized
328 on an SA sensor chip (GE Healthcare) with an analyte R_{max} of ~20 resonance units (RU).
329 Analyte measurements were performed at 25ºC and a flow rate of 40 μL/min. The chip surface
330 was regenerated between protein injections with a 40 μl 0.05% SDS injection. Data were
331 analysed using BIAevaluation 3.1 software (GE Healthcare). The kinetic parameters were
332 derived assuming a binding stoichiometry of 1 : 1.

333 **RNA competition assay**

334 250 nM NSP2 and NSP2-ΔC (RF) were pre-incubated with 10 nM 20mer AlexaFluor488-
335 labelled RNA (**Supplementary Table S1**) in binding buffer (50 mM NaCl, 25 mM HEPES pH
336 7.5). Fluorescence anisotropy measurements were performed in the presence of various
337 concentrations of unlabelled 20mer RNA in low-volume Greiner 384-well plates. Data were
338 recorded at 25ºC in a PHERAstar Plus multi-detection plate reader (BMG Labtech) equipped
339 with a fluorescence polarization optical module (λ_{ex} = 485 nm; λ_{em} = 520 nm). The data were
340 normalised and binding curves were fitted in Origin 9.0 using a Hill binding curve resulting in
341 R^2 values of 0.997 and 0.991 for NSP2 and NSP2-ΔC respectively.

342 **CTR peptide competition assay**

343 In order to maximise any potential competition between the CTR peptide and RNA, assays
344 were performed under conditions that favoured dissociation of NSP2-ΔC from RNA. The
345 binding assay was performed in PBS buffer (150 mM NaCl, 10 mM potassium phosphate, 3
346 mM potassium chloride). 25 nM AlexaFluor488-labelled RNA was incubated with 20-fold
347 excess NSP2-ΔC (500 nM, RF strain). After 30 minutes at room temperature (~25ºC), the CTR
348 peptide was added in 20-fold excess of NSP2-ΔC (i.e. 10 μM). To investigate direct CTR-RNA
349 interactions, 25 nM 10mer RNA was also co-incubated with 10 μM CTR peptide. Fluorescence
350 anisotropy measurements of RNA alone, RNA-NSP2-ΔC, RNA:NSP2-ΔC:CTR and RNA:CTR
351 were performed in triplicate as described above for RNA competition assays.

352 **Hydrogen-deuterium exchange mass spectrometry (HDX-MS)**

353 An automated HDX robot (LEAP Technologies, Ft Lauderdale, FL, USA) coupled to an Acquity
354 M-Class LC and HDX manager (Waters, UK) was used for all HDX-MS experiments.
355 Differential HDX-MS of NSP2 was performed using NSP2 (10 μM) or pre-incubated NSP2-
356 RNP complexes (10 μM + 2 μM 20mer RNA, **Supplementary Table S1**). 30 μl of protein-

357 containing solution was added to 135 µL deuterated buffer (10 mM potassium phosphate
358 buffer pD 8.0, 82% D_2O) and incubated at 4 °C for 0.5, 2, 30 or 120 min. After labelling, HDX
359 was quenched by adding 100 µL of quench buffer (10 mM potassium phosphate, 2 M Gdn-
360 HCl, pH 2.2) to 50 µL of the labelling reaction. 50 µL of the quenched sample was passed
361 through immobilised pepsin and aspergillopepsin columns (Affipro, Mratín, Czech Republic)
362 connected in series (20 °C) and the peptides were trapped on a VanGuard Pre-column
363 [Acquity UPLC BEH C18 (1.7 µm, 2.1 mm × 5 mm, Waters, UK)] for 3 min. The peptides were
364 separated using a C18 column (75 µm × 150 mm, Waters, UK) by gradient elution of 0–40%
365 (v/v) acetonitrile (0.1% v/v formic acid) in H_2O (0.3% v/v formic acid) over 7 min at 40 µL min^{-1}.
366 Peptides were detected using a Synapt G2Si mass spectrometer (Waters, UK). The mass
367 spectrometer was operated in $HDMS^E$ mode with the dynamic range extension enabled (data
368 independent analysis (DIA) coupled with IMS separation) were used to separate peptides prior
369 to CID fragmentation in the transfer cell. CID data were used for peptide identification and
370 uptake quantification was performed at the peptide level (as CID results in deuterium
371 scrambling). Data were analysed using PLGS (v3.0.2) and DynamX (*59*) (v3.0.0) software
372 (Waters, UK). Restrictions for peptides in DynamX were as follows: minimum intensity = 1000,
373 minimum products per amino acid = 0.3, max sequence length = 25, max ppm error = 5, file
374 threshold = 3. The software Deuteros (*60*) was used to identify peptides with statistically
375 significant increases/decreases in deuterium uptake (applying a 99 % confidence interval) and
376 to prepare Woods plots.

377 **UV-crosslinking-mass spectrometry with RBDmap**

378 10 μM NSP2 was incubated with 5'-A_{25}-S11 RNA in a final volume of 100 μl. NSP2-RNP
379 complexes were incubated at room temperature for 30 minutes and applied to a single well of
380 a 24-well plate. This 24-well plate was placed on an aluminium block cooled to 4°C within a
381 plastic container of ice and subjected to 6 rounds of UV irradiation (254 nm, 0.83 J cm^{-2} per
382 round) in a UVP CL-1000 Ultraviolet Crosslinker (Scientifix). Crosslinked RNP complexes
383 were digested by LysC (NEB, #P8109S) (500 ng per crosslinked RNP sample) overnight at
384 room temperature. Enrichment and identification of cross-linked peptides were performed
385 using the in vitro adaptation of the RBDmap protocol, as described in (*20*). Data analysis was
386 performed using the CrissCrosslinker R script, as described in (*20*).

387 **Circular dichroism (CD)**

388 CD experiments were performed in a Chirascan plus spectrometer (Applied Photophysics).
389 Samples were prepared by dialyzing protein solutions against 10 mM phosphate buffer pH
390 7.4, 50 mM sodium fluoride. Spectra were recorded over a wavelength range of 190–260 nm
391 with a bandwidth of 1 nm, step size of 1 nm and a path length of 1 mm. An average of three
392 scans were used for the final spectra.

393 **NSP2 (RF) threading and sequence alignment**

394 Alignment of NSP2(SA11) and NSP2(RF) sequences was performed using T-Coffee (*61*).
395 Threading of the NSP2(RF) sequence (based on the SA11 structure, PDB 1L9V) was
396 performed using I-TASSER (*62*).

397 **Cells and viruses**. MA104 (embryonic African green monkey kidney cells, ATCC® CRL-
398 2378) were cultured in Dulbecco's Modified Eagle's Medium (DMEM) (Life Technologies)
399 supplemented with 10% Fetal Bovine Serum (FBS) (Life Technologies). BHK-T7 cells (Baby
400 hamster kidney stably expressing T7 RNA polymerase) were cultured in Glasgow medium
401 supplemented with 5% FBS, 10% Tryptose Phosphate Broth (TPB, Sigma-Aldrich), 2% Non-
402 Essential Amino Acid (NEAA, Sigma) and 1% Glutamine. Recombinant simian RV strain SA11
403 NSP2 mutants were rescued using cDNA clones encoding the wild-type SA11 (G3P[2]) virus

404 with modifications, as previously described. Briefly, plasmids pT_7-VP1-SA11, pT_7-VP2-SA11,
405 pT_7-VP3-SA11, pT_7-VP4-SA11, pT_7-VP6-SA11, pT_7-VP7-SA11, pT_7-NSP1-SA11, pT_7-NSP2-
406 SA11, pT_7-NSP3-SA11, pT_7-NSP4-SA11, and pT_7-NSP5-SA11 (*11*) were used for
407 recombinant virus rescue in reverse genetics experiments. pT_7-NSP2 plasmid variants (NSP2-
408 EED, NSP2-AAA, and NSP2-6xHis) carrying mutations in gs8 were generated using Q5 site-
409 directed mutagenesis (NEB), using mutagenesis primers (Supplementary Table S1). To
410 rescue recombinant RV strain SA11, monolayers of BHK-T7 cells (4×10^5) cultured in 12-well
411 plates were co-transfected using 2.5 µL of TransIT-LT1 transfection reagent (Mirus) per
412 microgram of DNA plasmid. Each mixture comprised 0.8 µg of SA11 rescue plasmids: pT_7-
413 VP1, pT_7-VP2, pT_7-VP3, pT_7-VP4, pT_7-VP6, pT_7-VP7, pT_7-NSP1, pT_7-NSP3, pT_7-NSP4, and
414 2.4 µg of pT_7-NSP2 and pT_7-NSP5 (*11*, *63*). Additional 0.8 µg of pcDNA3-NSP2 and 0.8 µg
415 of pcDNA3-NSP5, encoding NSP2 and NSP5 proteins, were also co-transfected to increase
416 the virus rescue efficiencies. At 24 h post-transfection, MA104 cells (5×10^4 cells) were added
417 to the transfected cells and co-cultured for 72 hours in FBS-free medium supplemented with
418 trypsin (0.5 µg/mL, Sigma Aldrich). After incubation, transfected cells were lysed by repeated
419 freeze-thawing and 0.2 ml of the lysate was transferred to a fresh MA104 cell monolayer. After
420 adsorption at 37°C for 1 hour, followed by a 5 min wash with PBS, cells were further cultured
421 for 4 days in FBS-free DMEM supplemented with 0.5 µg/mL trypsin until a clear cytopathic
422 effect (CPE) was visible. For AAA mutant, where CPE was not observed after 4 days of
423 incubation, cells were harvested and lysed by freeze-thawing, and the clarified lysates were
424 used for two additional blind virus passages, during which RNA samples were extracted from
425 these lysates for further verification of viral replication by RT-PCR using gs8-specific primers
426 (Supplementary Table S1). These recombinant viruses were verified by Sanger sequencing
427 of the gs8-NSP2 RT-PCR products (GenBank IDs: MW074066, MW074067, MW074067).
428

429 *Authors' contribution*: J.B.K.B., K.B., L.V., E.G., A.C. and A.B. designed and carried out
430 experiments, and analyzed data. J.B., K.B., A.C. and A.B. jointly wrote the manuscript. R.T.,
431 D.C.L., C.D. contributed novel analytical tools. J.B. collected and analyzed EM data. A.C.
432 collected and analyzed HDX data. K.B. and A.B. collected and analysed single-molecule
433 fluorescence data. A.B. managed the project. All authors contributed ideas, discussed the
434 results and were involved in writing of the manuscript.
435

436 **Acknowledgements**

437 The authors would like to thank Prof Ben Luisi, Dr Anders Barth and Dr Chris Hill for their
438 valuable comments and suggestions. We would like to thank Dr Guido Papa and Dr Oscar
439 Burrone for their generous gift of pT7 constructs used for rescuing recombinant rotaviruses.
440

441 Funding sources: A.B. acknowledges support from a Sir Henry Dale Fellowship jointly funded
442 by the Wellcome Trust and the Royal Society (Grant Number: 213437/Z/18/Z); Biotechnology
443 and Biological Sciences Research Council (BBSRC) White Rose DTP [BB/M011151/1 to
444 J.P.K.B.]; European Regional Development Fund [CZ.02.1.01/0.0/0.0/15_003/0000441 to
445 R.T.]; A.N.C. acknowledges support from a Sir Henry Dale Fellowship jointly funded by the
446 Wellcome Trust and the Royal Society (Grant Number 220628/Z/20/Z) and a University
447 Academic Fellowship from the University of Leeds. E.H.G. holds a Biomedicine Discovery
448 Scholarship and is an EMBL-Australia PhD student. C.D. is an EMBL-Australia Group Leader

and acknowledges support from the ARC (DP190103407) and the NHMRC (APP1162921 & APP1184637).

Deutsche Forschungsgemeinschaft SFB1032 (Project B3) [to D.C.L.] and the Ludwig-Maximilians-Universität, München through the Center for NanoScience (CeNS) and the LMUinnovativ initiative BioImaging Network (BIN) (to D.C.L.).

Funding from the BBSRC (BB/M012573/1) to purchase HDX-MS instrumentation is acknowledged.

Funding for open access charge: Wellcome Trust.

461 ## References

462 1. S. McDonald, M. I. Nelson, P. E. Turner, J. T. Patton, Reassortment in segmented
463 RNA viruses: mechanisms and outcomes. *Nat. Rev. Microbiol.* **14**, 448–460 (2016).
464 2. S. McDonald, J. T. Patton, Assortment and packaging of the segmented rotavirus
465 genome. *Trends Microbiol.* **19**, 136–144 (2011).
466 3. A. Borodavka, U. Desselberger, J. T. Patton, Genome packaging in multi-segmented
467 dsRNA viruses: distinct mechanisms with similar outcomes. *Curr. Opin. Virol.* **33**,
468 106–112 (2018).
469 4. J. P. K. Bravo, A. Borodavka, A. Barth, A. N. Calabrese, P. Mojzes, J. J. B. Cockburn,
470 D. C. Lamb, R. Tuma, Stability of local secondary structure determines selectivity of
471 viral RNA chaperones. *Nucleic Acids Res.*, 293191 (2018).
472 5. L. R. Newburn, K. A. White, Trans-Acting RNA–RNA Interactions in Segmented RNA
473 Viruses. *Viruses*. **11**, 751 (2019).
474 6. Z. F. Taraporewala, J. T. Patton, Nonstructural proteins involved in genome
475 packaging and replication of rotaviruses and other members of the Reoviridae. *Virus*
476 *Res.* **101** (2004), pp. 57–66.
477 7. H. Jayaram, Z. F. Taraporewala, J. T. Patton, B. V. V. Prasad, Rotavirus protein
478 involved in genome replication and packaging exhibits a HIT-like fold. *Nature*. **417**,
479 311–5 (2002).
480 8. Z. F. Taraporewala, J. T. Patton, D. Chen, J. T. Patton, Identification and
481 Characterization of the Helix-Destabilizing Activity of Rotavirus Nonstructural Protein
482 NSP2. *J. Virol.* **75**, 4519–4527 (2001).
483 9. Z. F. Taraporewala, X. Jiang, R. Vasquez-Del Carpio, H. Jayaram, B. V. V. Prasad, J.
484 T. Patton, Structure-function analysis of rotavirus NSP2 octamer by using a novel
485 complementation system. *J. Virol.* **80**, 7984–7994 (2006).
486 10. L. S. Silvestri, Z. F. Taraporewala, J. T. Patton, Rotavirus Replication: Plus-Sense
487 Templates for Double-Stranded RNA Synthesis Are Made in Viroplasms. *J. Virol.* **78**,
488 7763–7774 (2004).
489 11. Y. Kanai, S. Komoto, T. Kawagishi, R. Nouda, N. Nagasawa, M. Onishi, Y. Matsuura,
490 K. Taniguchi, T. Kobayashi, Entirely plasmid-based reverse genetics system for
491 rotaviruses. *Proc. Natl. Acad. Sci.*, 201618424 (2017).
492 12. U. Desselberger, At last : a fully tractable, plasmid only based reverse genetics
493 system for rotavirus. **12**, 519–524, *Future Virology, **12***, 9 (2017).
494 13. U. Desselberger, Reverse genetics of rotavirus. *Proc. Natl. Acad. Sci. U. S. A.* **114**,
495 2106–2108 (2017).
496 14. L. Hu, S. E. Crawford, J. M. Hyser, M. K. Estes, B. V. V. Prasad, Rotavirus non-
497 structural proteins: Structure and function. *Curr. Opin. Virol.* **2**, 380–388 (2012).
498 15. J. M. Criglar, R. Anish, L. Hu, S. E. Crawford, B. Sankaran, B. V. V. Prasad, M. K.
499 Estes, Phosphorylation cascade regulates the formation and maturation of rotaviral
500 replication factories. *Proc. Natl. Acad. Sci. U. S. A.* **115**, E12015–E12023 (2018).
501 16. J. M. Criglar, L. Hu, S. E. Crawford, J. M. Hyser, J. R. Broughman, B. V. V. Prasad,
502 M. K. Estes, A Novel Form of Rotavirus NSP2 and Phosphorylation-Dependent
503 NSP2-NSP5 Interactions Are Associated with Viroplasm Assembly. *J. Virol.* **88**, 786–
504 98 (2014).
505 17. A. Borodavka, E. C. Dykeman, W. Schrimpf, D. C. Lamb, Protein-mediated RNA
506 folding governs sequence-specific interactions between rotavirus genome segments.
507 *Elife*. **6**, 1–22 (2017).
508 18. L. Hu, D.-C. Chow, J. T. Patton, T. Palzkill, M. K. Estes, B. V. V. Prasad,
509 Crystallographic Analysis of Rotavirus NSP2-RNA Complex Reveals Specific
510 Recognition of 5' GG Sequence for RTPase Activity. *J. Virol.* **86**, 10547–10557

511 (2012).
512 19. E. Haustein, P. Schwille, Single-molecule spectroscopic methods. *Curr. Opin. Struct.*
513 *Biol.* **14** (2004), pp. 531–540.
514 20. Q. Zhang, N. J. McKenzie, R. Warneford-Thomson, E. H. Gail, S. F. Flanigan, B. M.
515 Owen, R. Lauman, V. Levina, B. A. Garcia, R. B. Schittenhelm, R. Bonasio, C.
516 Davidovich, RNA exploits an exposed regulatory site to inhibit the enzymatic activity
517 of PRC2. *Nat. Struct. Mol. Biol.* **26**, 237–247 (2019).
518 21. A. Castello, B. Fischer, C. K. Frese, R. Horos, A. M. Alleaume, S. Foehr, T. Curk, J.
519 Krijgsveld, M. W. Hentze, Comprehensive Identification of RNA-Binding Domains in
520 Human Cells. *Mol. Cell.* **63**, 696–710 (2016).
521 22. M. J. Conley, M. McElwee, L. Azmi, M. Gabrielsen, O. Byron, I. G. Goodfellow, D.
522 Bhella, Calicivirus VP2 forms a portal-like assembly following receptor engagement.
523 *Nature*. **565** (2019), pp. 377–381.
524 23. S. H. W. Scheres, *Processing of Structurally Heterogeneous Cryo-EM Data in*
525 *RELION* (Elsevier Inc., ed. 1, 2016; http://dx.doi.org/10.1016/bs.mie.2016.04.012),
526 vol. 579.
527 24. D. Lyumkis, Challenges and opportunities in cryo-EM single-particle analysis. *J. Biol.*
528 *Chem.* **294**, 5181–5197 (2019).
529 25. R. Vasquez-Del Carpio, F. D. Gonzalez-Nilo, G. Riadi, Z. F. Taraporewala, J. T.
530 Patton, Histidine Triad-like Motif of the Rotavirus NSP2 Octamer Mediates both
531 RTPase and NTPase Activities. *J. Mol. Biol.* **362**, 539–554 (2006).
532 26. Z. F. Taraporewala, D. Chen, J. T. Patton, Multimers Formed by the Rotavirus
533 Nonstructural Protein NSP2 Bind to RNA and Have Nucleoside Triphosphatase
534 Activity. *J. Virol.* **73**, 9934–9943 (1999).
535 27. D. Thirumalai, S. A. Woodson, Kinetics of Folding of Proteins and RNA. *Acc. Chem.*
536 *Res.* **29**, 433–439 (1996).
537 28. M. A. Ditzler, D. Rueda, J. Mo, K. Håkansson, N. G. Walter, A rugged free energy
538 landscape separates multiple functional RNA folds throughout denaturation. *Nucleic*
539 *Acids Res.* **36**, 7088–7099 (2008).
540 29. H. F. Noller, RNA Structure: Reading the Ribosome. *Science (80-.).* **309**, 1508–1514
541 (2005).
542 30. P. Bieniasz, A. Telesnitsky, *Annu. Rev. Virol.*, in press, doi:10.1146/annurev-virology-
543 092917-043448.
544 31. D. Herschlag, RNA chaperones and the folding problem. *J. Biol. Chem.* **270**, 20871–
545 20874 (1995).
546 32. R. Russell, RNA misfolding and the action of chaperones. *Front. Biosci.* **13**, 1–20
547 (2008).
548 33. I. Jarmoskaite, R. Russell, DEAD-box proteins as RNA helicases and chaperones.
549 *Wiley Interdiscip. Rev. RNA*. **2** (2011), pp. 135–152.
550 34. L. Rajkowitsch, D. Chen, S. Stampfl, K. Semrad, C. Waldsich, O. Mayer, M. F.
551 Jantsch, R. Konrat, U. Bläsi, R. Schroeder, RNA chaperones, RNA annealers and
552 RNA helicases. *RNA Biol.* **4** (2007), pp. 118–130.
553 35. Z. F. Taraporewala, J. T. Patton, Identification and Characterization of the Helix-
554 Destabilizing Activity of Rotavirus Nonstructural Protein NSP2. *J. Virol.* **75**, 4519–
555 4527 (2001).
556 36. A. Borodavka, J. Ault, P. G. Stockley, R. Tuma, Evidence that avian reovirus σNS is
557 an RNA chaperone: implications for genome segment assortment. *Nucleic Acids Res.*
558 **43**, 7044–7057 (2015).
559 37. O. Mayer, L. Rajkowitsch, C. Lorenz, R. Konrat, R. Schroeder, RNA chaperone
560 activity and RNA-binding properties of the E. coli protein StpA. *Nucleic Acids Res.* **35**,
561 1257–1269 (2007).

562 38. A. Belfetmi, L. Zargarian, C. Tisné, D. Sleiman, N. Morellet, E. Lescop, O. Maskri, B.
563 René, Y. Mély, P. Fossé, O. Mauffret, Insights into the mechanisms of RNA
564 secondary structure destabilization by the HIV-1 nucleocapsid protein. *Rna*. **22**, 506–
565 517 (2016).
566 39. J. Vogel, B. F. Luisi, Hfq and its constellation of RNA. *Nat. Rev. Microbiol.* **9** (2011),
567 pp. 578–589.
568 40. A. Santiago-Frangos, S. A. Woodson, Hfq chaperone brings speed dating to bacterial
569 sRNA. *Wiley Interdiscip. Rev. RNA*. **9**, 1–16 (2018).
570 41. S. A. Woodson, S. Panja, A. Santiago-Frangos, Proteins That Chaperone RNA
571 Regulation. *Microbiol. Spectr.* **113**, E6089–E6096 (2018).
572 42. A. Santiago-Frangos, K. Kavita, D. J. Schu, S. Gottesman, S. A. Woodson, C-terminal
573 domain of the RNA chaperone Hfq drives sRNA competition and release of target
574 RNA. *Proc. Natl. Acad. Sci.* **113**, E6089–E6096 (2016).
575 43. A. Santiago-Frangos, K. S. Fröhlich, J. R. Jeliazkov, E. M. Małecka, G. Marino, J. J.
576 Gray, B. F. Luisi, S. A. Woodson, S. W. Hardwick, Caulobacter crescentus Hfq
577 structure reveals a conserved mechanism of RNA annealing regulation. *Proc. Natl.*
578 *Acad. Sci. U. S. A.*, 1–10 (2019).
579 44. A. Santiago-Frangos, J. R. Jeliazkov, J. J. Gray, S. A. Woodson, Acidic C-terminal
580 domains autoregulate the RNA chaperone Hfq. *Elife*. **6**, 1–25 (2017).
581 45. J. Zivanov, T. Nakane, B. Forsberg, D. Kimanius, W. J. H. J. Hagen, E. Lindahl, S. H.
582 W. Scheres, E. H. Egelman, J. Zivanov, T. Nakane, B. O. rn Forsberg, D. Kimanius,
583 W. J. H. J. Hagen, E. Lindahl, S. H. W. Scheres, RELION-3: new tools for automated
584 high-resolution cryo-EM structure determination. *Elife*, 421123 (2018).
585 46. S. Q. Zheng, E. Palovcak, J. P. Armache, K. A. Verba, Y. Cheng, D. A. Agard,
586 MotionCor2: Anisotropic correction of beam-induced motion for improved cryo-
587 electron microscopy. *Nat. Methods*. **14**, 331–332 (2017).
588 47. K. Zhang, Gctf: Real-time CTF determination and correction. *J. Struct. Biol.* **193**, 1–12
589 (2016).
590 48. T. D. Goddard, C. C. Huang, E. C. Meng, E. F. Pettersen, G. S. Couch, J. H. Morris,
591 T. E. Ferrin, UCSF ChimeraX: Meeting modern challenges in visualization and
592 analysis. *Protein Sci.* **27**, 14–25 (2018).
593 49. R. T. Kidmose, J. Juhl, P. Nissen, T. Boesen, J. L. Karlsen, B. P. Pedersen,
594 Namdinator - Automatic molecular dynamics flexible fitting of structural models into
595 cryo-EM and crystallography experimental maps. *IUCrJ*. **6**, 526–531 (2019).
596 50. P. Emsley, K. Cowtan, Coot: Model-building tools for molecular graphics. *Acta*
597 *Crystallogr. Sect. D Biol. Crystallogr.* **60**, 2126–2132 (2004).
598 51. P. V. Afonine, B. K. Poon, R. J. Read, O. V. Sobolev, T. C. Terwilliger, A.
599 Urzhumtsev, P. D. Adams, Real-space refinement in PHENIX for cryo-EM and
600 crystallography. *Acta Crystallogr. Sect. D Struct. Biol.* **74**, 531–544 (2018).
601 52. V. B. Chen, W. B. Arendall, J. J. Headd, D. A. Keedy, R. M. Immormino, G. J. Kapral,
602 L. W. Murray, J. S. Richardson, D. C. Richardson, MolProbity: All-atom structure
603 validation for macromolecular crystallography. *Acta Crystallogr. Sect. D Biol.*
604 *Crystallogr.* **66**, 12–21 (2010).
605 53. H. Ashkenazy, S. Abadi, E. Martz, O. Chay, I. Mayrose, T. Pupko, N. Ben-Tal,
606 ConSurf 2016: an improved methodology to estimate and visualize evolutionary
607 conservation in macromolecules. *Nucleic Acids Res.* **44**, W344–W350 (2016).
608 54. G. Crooks, G. Hon, J. Chandonia, S. Brenner, WebLogo: a sequence logo generator.
609 *Genome Res*. **14**, 1188–1190 (2004).
610 55. N. A. Baker, D. Sept, S. Joseph, M. J. Holst, J. A. McCammon, Electrostatics of
611 nanosystems: Application to microtubules and the ribosome. *Proc. Natl. Acad. Sci. U.*
612 *S. A.* **98**, 10037–10041 (2001).

56. V. Kudryavtsev, M. Sikor, S. Kalinin, D. Mokranjac, C. A. M. Seidel, D. C. Lamb, Combining MFD and PIE for accurate single-pair förster resonance energy transfer measurements. *ChemPhysChem*. **13**, 1060–1078 (2012).
57. T. Cordes, J. Vogelsang, P. Tinnefeld, On the mechanism of trolox as antiblinking and antibleaching reagent. *J. Am. Chem. Soc.* **131**, 5018–5019 (2009).
58. W. Schrimpf, A. Barth, J. Hendrix, D. C. Lamb, Computational Tool PAM : A Framework for Integrated Analysis of Imaging , Single-Molecule , and Ensemble Fluorescence Data. *Biophysj*. **114**, 1518–1528 (2018).
59. A. Cryar, K. Groves, M. Quaglia, Online Hydrogen-Deuterium Exchange Traveling Wave Ion. *J. Am. Soc. Mass Spectrom.* **28**, 1192–1202 (2017).
60. A. M. C. Lau, Z. Ahdash, C. Martens, A. Politis, Deuteros: Software for rapid analysis and visualization of data from differential hydrogen deuterium exchange-mass spectrometry. *Bioinformatics*. **35**, 3171–3173 (2019).
61. P. Di Tommaso, S. Moretti, I. Xenarios, M. Orobitg, A. Montanyola, J. M. Chang, J. F. Taly, C. Notredame, T-Coffee: A web server for the multiple sequence alignment of protein and RNA sequences using structural information and homology extension. *Nucleic Acids Res.* **39**, 13–17 (2011).
62. A. Roy, A. Kucukural, Y. Zhang, I-TASSER: A unified platform for automated protein structure and function prediction. *Nat. Protoc.* **5**, 725–738 (2010).
63. G. Papa, L. Venditti, F. Arnoldi, E. M. Schraner, C. Potgieter, A. Borodavka, C. Eichwald, O. R. Burrone, Recombinant rotaviruses rescued by reverse genetics reveal the role of NSP5 hyperphosphorylation in the assembly of viral factories. *J. Virol.* **94**, 1–23 (2019).

Supplementary Information

Structural basis of rotavirus RNA chaperone displacement and RNA annealing

Jack P. K. Bravo, Kira Bartnik, Luca Venditti, Emma H. Gail, Chen Davidovich, Don C Lamb, Roman Tuma, Antonio N. Calabrese, Alexander Borodavka

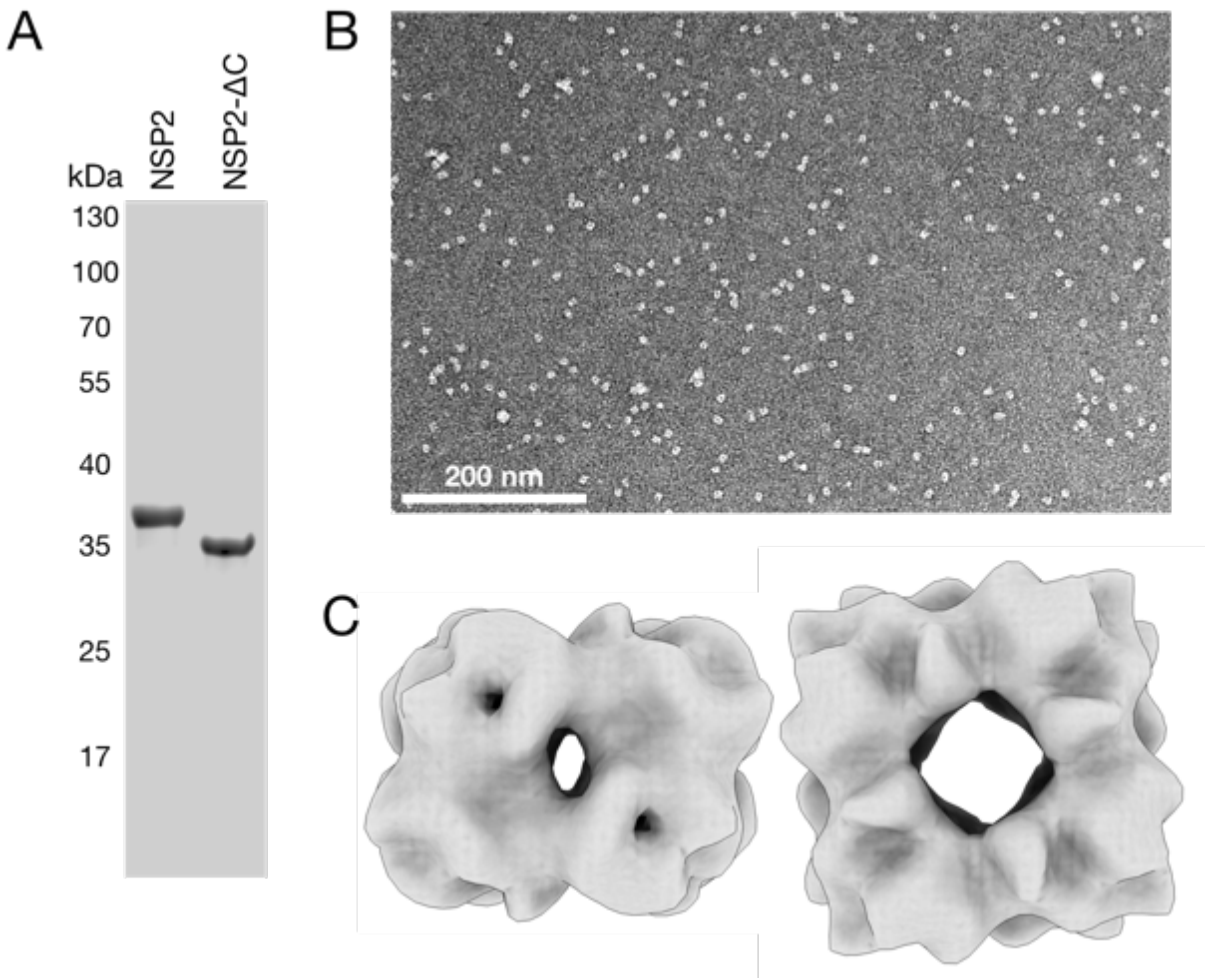

650

651 **Supplementary Figure S1. NSP2–ΔC variant assembles into octamers.**

652 **A:** SDS-PAGE of purified NSP2 and NSP2-ΔC. **B:** Representative negative stain EM
653 micrograph of NSP2-ΔC **C:** 3D reconstruction of NSP2-ΔC.

654

655

656

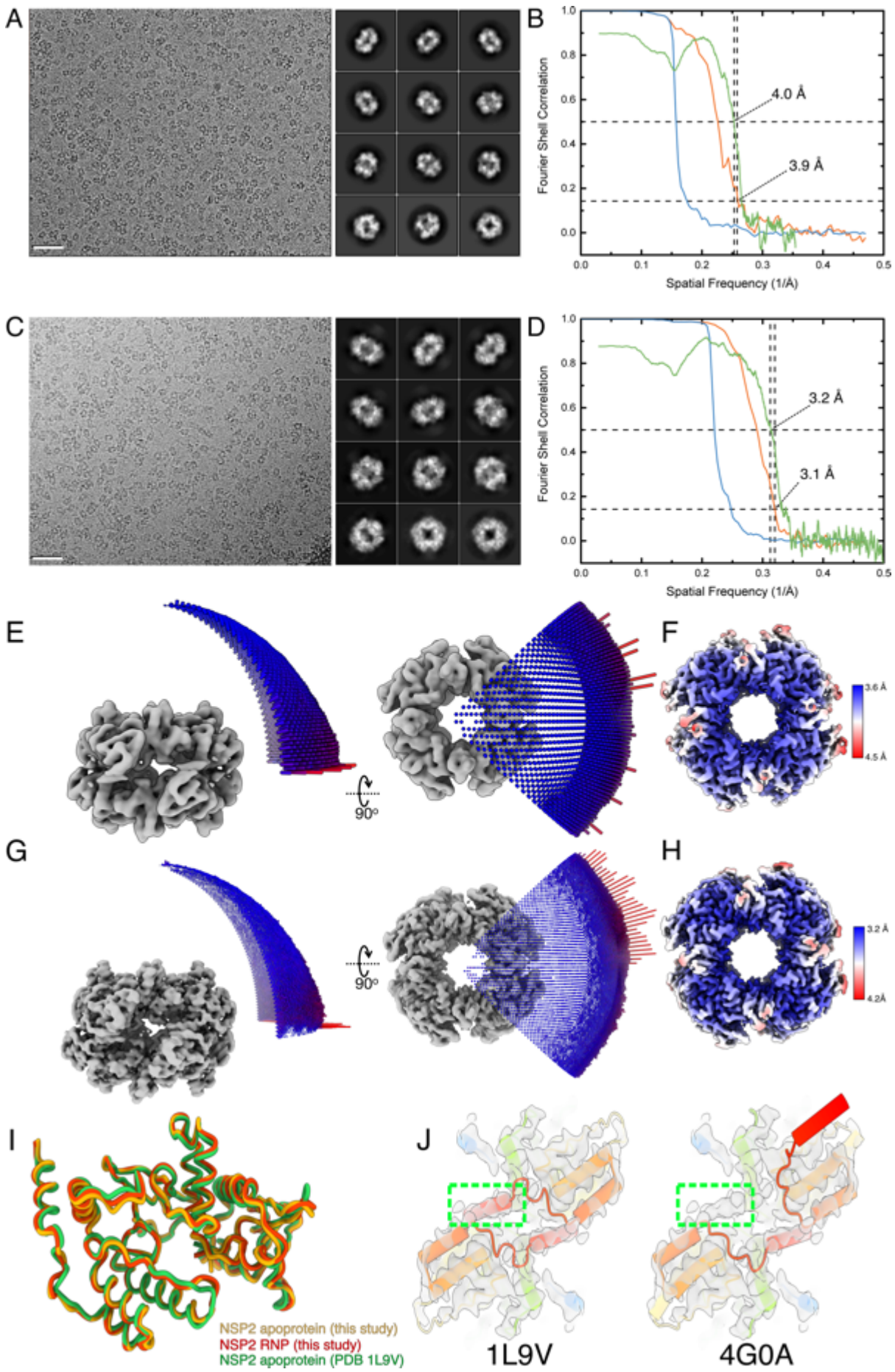
A
B
Fourier Shell Correlation
Spatial Frequency (1/Å)
4.0 Å
3.9 Å
C
D
3.2 Å
3.1 Å
E
F
3.6 Å
4.5 Å
90°
G
H
3.2 Å
4.2Å
I
NSP2 apoprotein (this study)
NSP2 RNP (this study)
NSP2 apoprotein (PDB 1L9V)
J
1L9V
4G0A

657

Supplementary Figure S2. Cryo-EM structure determination of the NSP2 apoprotein and the NSP2-RNP complex. A: A representative cryo-EM micrograph of the NSP2 apoprotein and corresponding 2D class averages. **B:** The Fourier shell correlation (FSC) curves for the overall NSP2 apoprotein map (orange) and phase randomized map (blue). The map has a final resolution of 3.9 Å. Model versus map FSC curve (green) indicates a model resolution of 4.0 Å. **C:** A representative cryo-EM micrograph of the NSP2 RNP complex and corresponding 2D class averages. **D:** The Fourier shell correlation (FSC) curves for the overall NSP2-RNP complex map (orange) and phase randomized map (blue). Map has a final resolution of 3.2 Å. Model versus map FSC curve (green) indicates a model resolution of 3.1 Å. **E & G:** Euler angle distribution of particles corresponding to NSP2 apoprotein and NSP2-RNP reconstructions. The cylinder height and color represent the number of particles (blue to red – low to high). A D4 symmetry has been applied for both the NSP2 apoprotein and the NSP2-RNP complex reconstructions. **F & H:** NSP2 apoprotein (F) and NSP2-RNP complex (H) reconstructions colored by local resolution as calculated by Relion. **I:** Aligned models of the NSP2 apoprotein and the NSP2-RNP complex built from reconstructions presented in this study (yellow and red, respectively), and a previous crystal structure of the NSP2 apoprotein (PDB ID 1L9V) (green). Alignment of the apoprotein and RNP models from this study to 1L9V had an RMSD of 1.081 Å and 0.772 Å, respectively. The two models from this study had an RMSD of 0.742 Å. **J:** Fitting of previous NSP2 crystal structures into the NSP2 apoprotein cryo-EM density map. The “open” NSP2 conformation (PDB 4G0A) has the CTR flipped outwards, while the “closed” conformation (PDB 1L9V) has the CTR making contacts with the $NSP2_{core}$. The open conformation is not represented by the cryo-EM map, as the CTH density is clearly visible and localized to the $NSP2_{core}$. The green box highlights the cryo-EM density corresponding to the C-terminus.

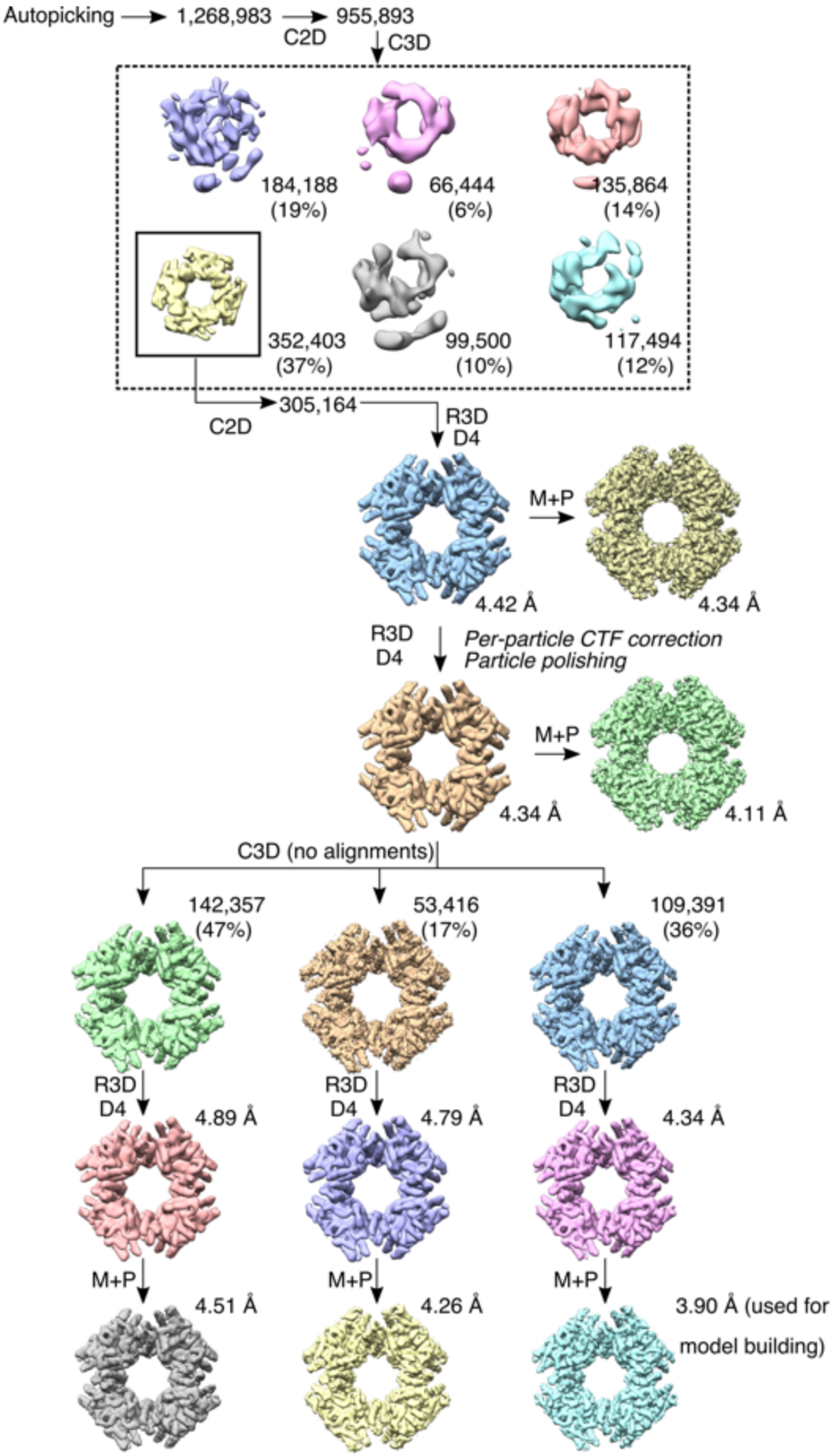
Autopicking
1,268,983
C2D
955,893
C3D
184,188
(19%)
66,444
(6%)
135,864
(14%)
352,403
(37%)
99,500
(10%)
117,494
(12%)
C2D
305,164
R3D
D4
M+P
4.42 Å
4.34 Å
R3D
D4
Per-particle CTF correction
Particle polishing
M+P
4.34 Å
4.11 Å
C3D (no alignments)
142,357
(47%)
53,416
(17%)
109,391
(36%)
R3D
D4
4.89 Å
R3D
D4
4.79 Å
R3D
D4
4.34 Å
M+P
4.51 Å
M+P
4.26 Å
M+P
3.90 Å (used for
model building)

686

Supplementary Figure S3. The NSP2 apoprotein cryo-EM image-processing workflow. The image processing workflow used to determine the 3D reconstruction of the NSP2 apoprotein. Initial rounds of 2D classification (C2D) and 3D classification (C3D) were performed using Fast Subsets and image alignments with 25 iterations. The highest quality 3D class average was subjected to further 2D classification without fast subsets, and used for 3D refinement (R3D) with D4 symmetry imposed. After per-particle CTF correction and particle polishing, further 3D classification was performed without fast subsets, and without performing image alignment. 3D reconstructions were ultimately subjected to masking (M) and post-processing (P).

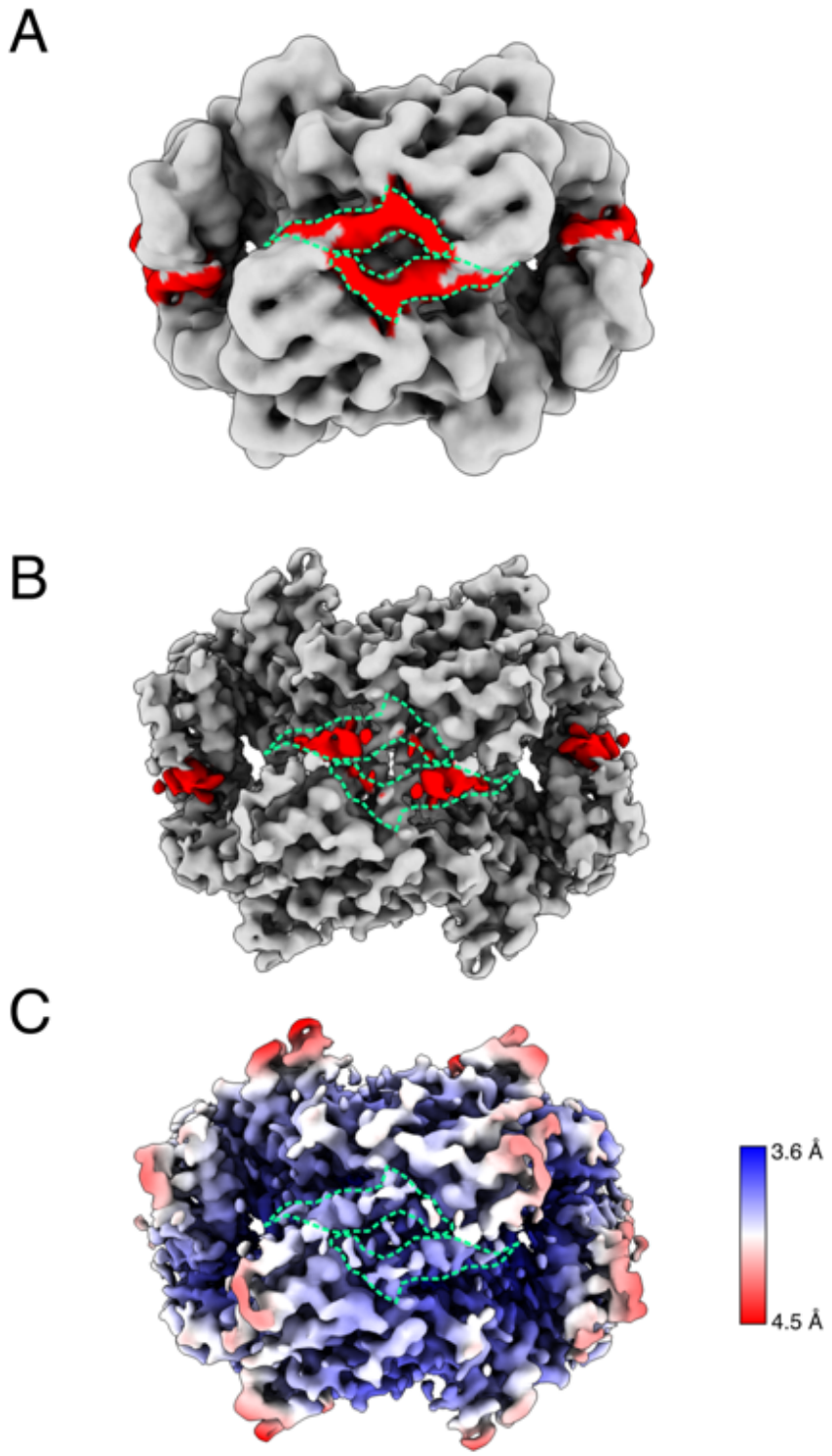

697
698 **Supplementary Figure S4. Cryo-EM density of the flexible linker within the CTR.**
699 **A & B:** Unsharpened (A) and sharpened (B) NSP2 apoprotein cryo-EM density maps.
700 Density corresponding to the CTR is shown in red (green outline). Linker density is
701 diffuse in the sharpened map (B). **C:** Local resolution of NSP2 with the CTR outlined
702 in green.

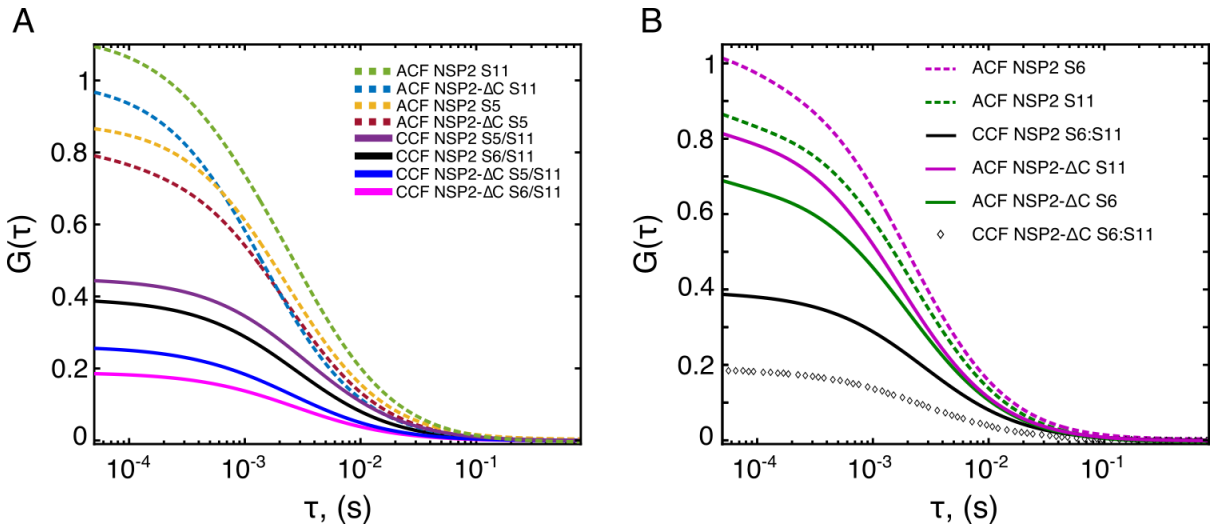

Supplementary Figure S5. Fluorescence cross-correlation spectroscopy (FCCS) and Fluorescence Correlation Spectroscopy (FCS) measurements of NSP2 and NSP2-ΔC. A: Autocorrelation functions (ACFs) of rotavirus (RV) segments S5 and S11 in the presence of NSP2 and NSP2-ΔC (dashed lines). Cross-correlation functions (CCFs) (bold lines) of segments S5 and S11 in the presence of NSP2 (burgundy) and NSP2-ΔC (navy) and segments S6 and S11 in the presence of NSP2 (black) and NSP2-ΔC (magenta). **B:** ACFs and CCFs of S6 and S11 in the presence of NSP2 and NSP2-ΔC. Dashed, colored lines correspond to ACFs of WT NSP2 in complex with RV S6 and S11 RNAs, and continuous, colored lines correspond to ACFs of NSP2-ΔC in complex with RV S6 and S11 RNAs. Continuous black line and diamonds correspond to CCFs of both S6 and S11 in the presence of NSP2 and NSP2-ΔC, respectively.

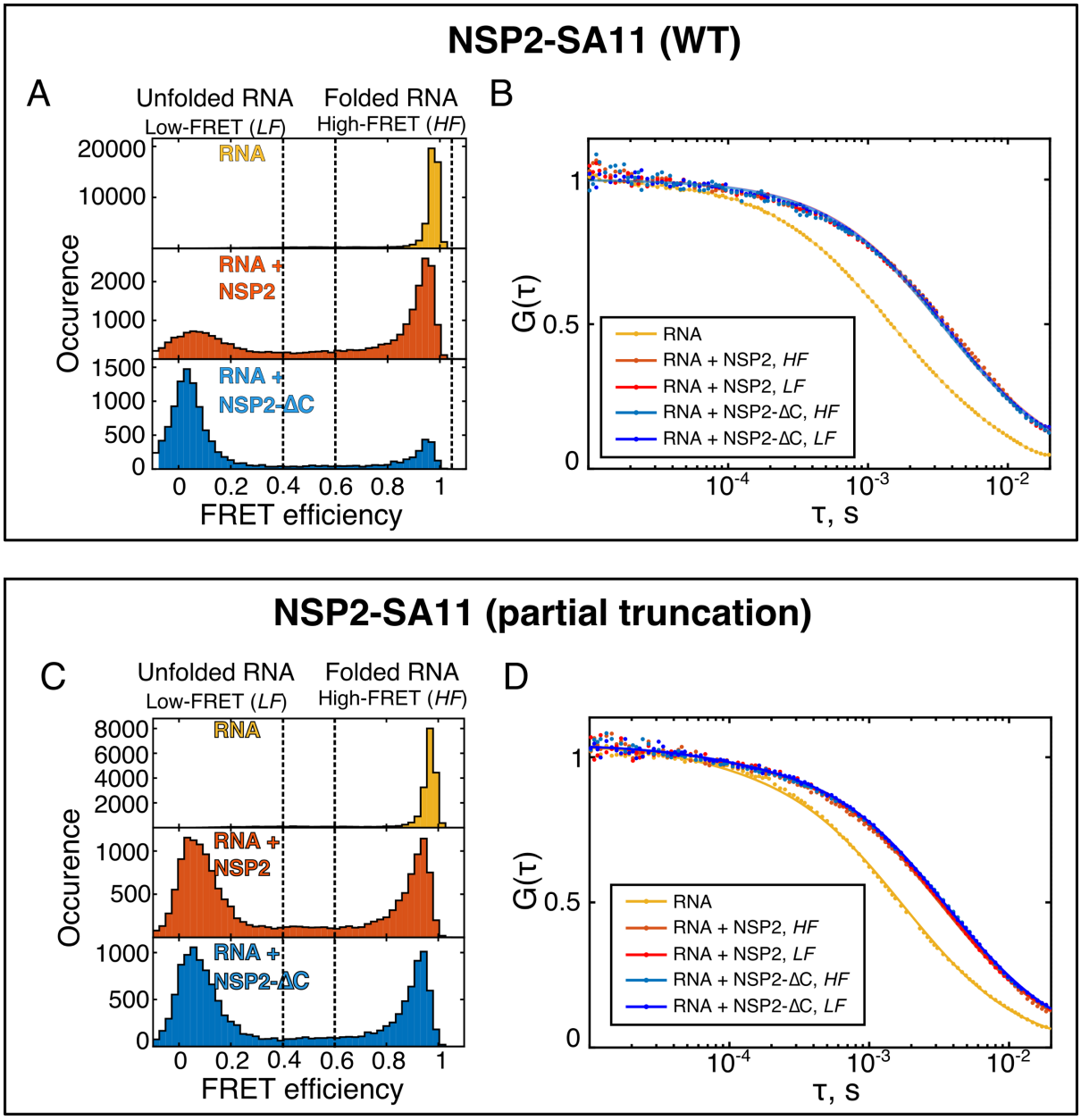

Supplementary Figure S6. SmFRET and burstwise FCS analysis of stem-loop unwinding by NSP2 variants. A & B: SmFRET histograms (**A**) and corresponding burstwise FCS analysis (**B**) of the NSP2 strain SA11 and NSP2 (SA11)-ΔC. **C & D** SmFRET histograms (**C**) and corresponding burstwise FCS analysis (**D**) of the NSP2 SA11 strain and a partially truncated NSP2 (lacking the unstructured residues 314-316). These residues are not essential for virus replication (*9*), and do not contribute to RNA unwinding.

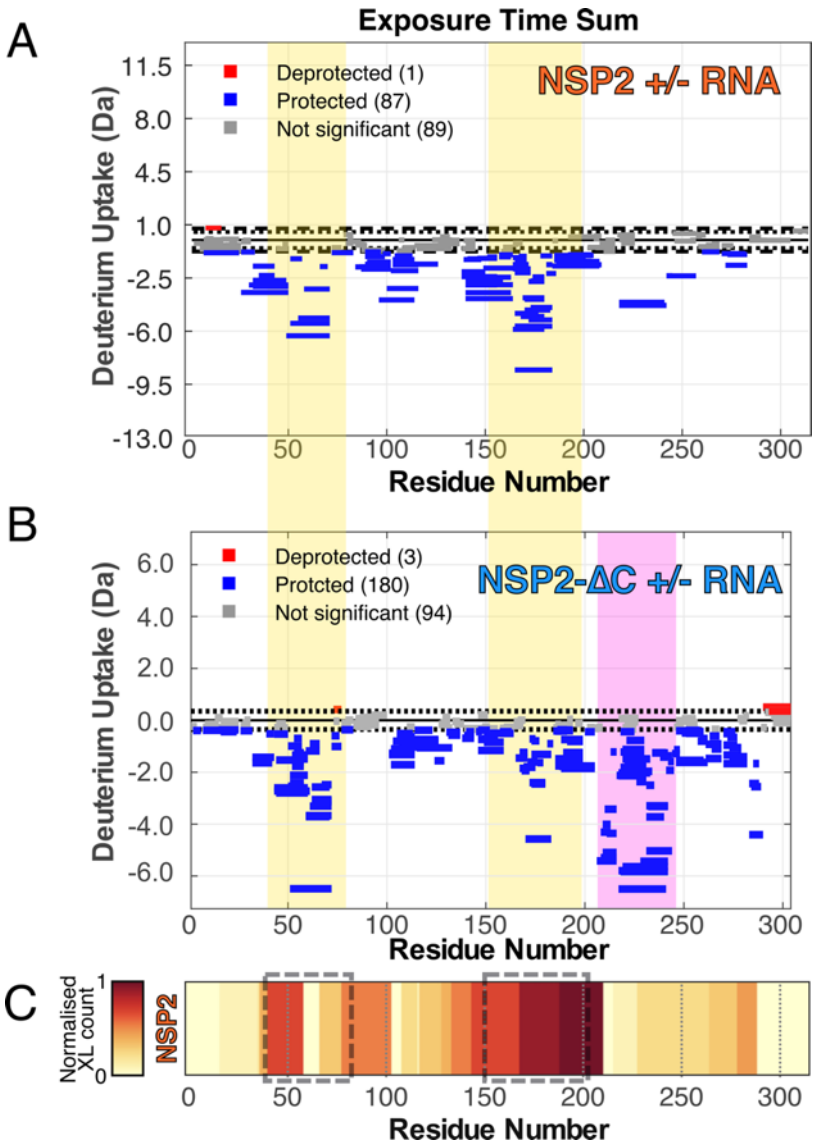

Supplementary Figure S7. A & B: Woods plots showing summed differences in deuterium uptake in NSP2 **(A)** and NSP2-ΔC **(B)** over all timepoints, comparing the apoproteins with their respective RNP complex. Regions corresponding to flexible loops located within the polar, equatorial groove of NSP2 are denoted by yellow shading. In NSP2-ΔC, the magenta box denotes residues that would be otherwise buried underneath the CTR. This includes R240. **C**: A heatmap of crosslinked peptides mapped onto the NSP2 sequence (plotted as counts per residue). Residues corresponding to flexible loops within the equatorial grove are denoted by grey boxes. These regions correspond to the yellow-shaded areas in the above Woods plots.

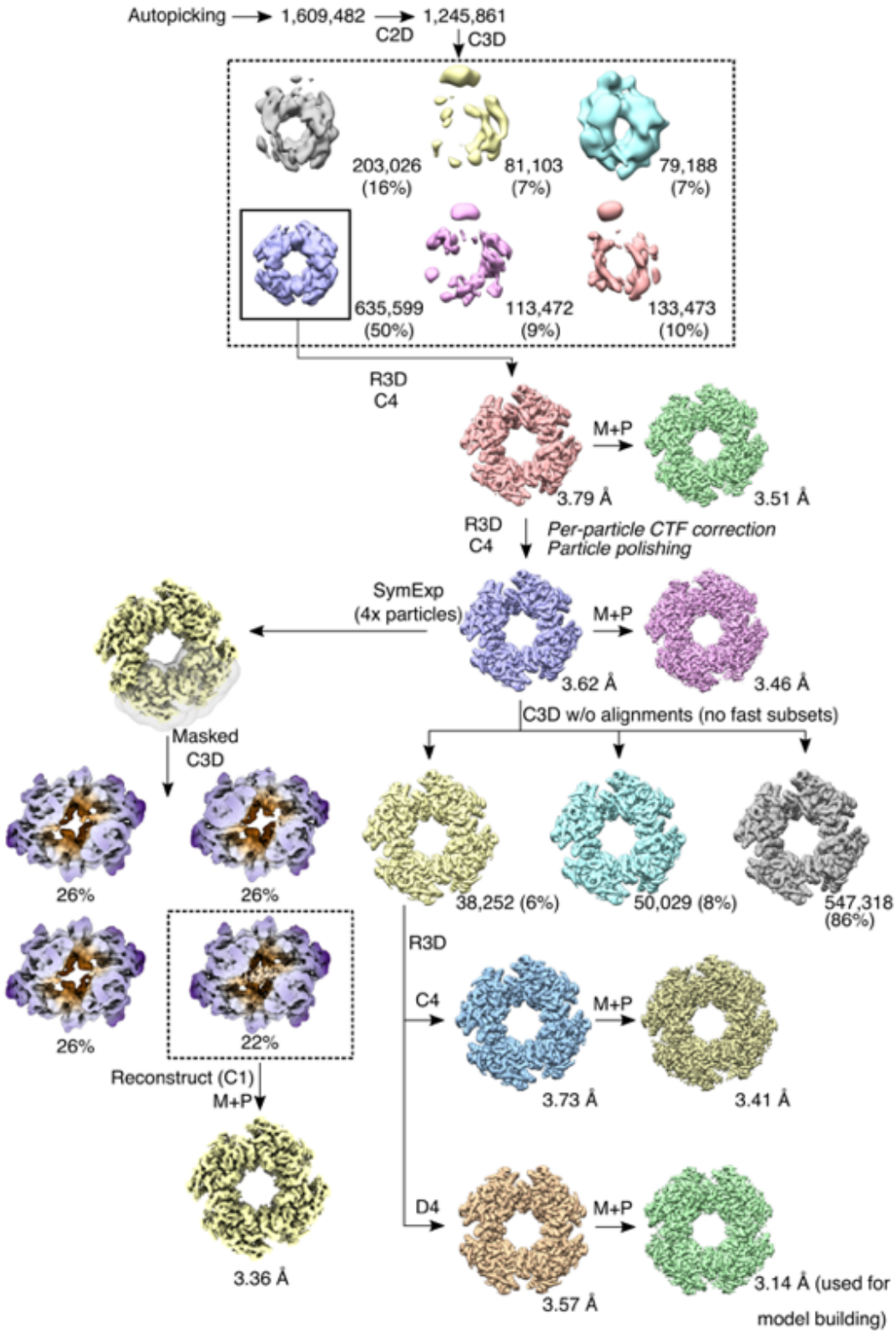

Supplementary Figure S8. The NSP2 RNP cryo-EM image-processing workflow. The image processing scheme used to determine the 3D reconstruction of NSP2 RNP. Initial 2D and 3D classifications (C2D and C3D, respectively) were performed with fast subsets. Purple: Focused classification of NSP2-RNP demonstrate the existence of an RNA-binding groove with variable occupancy. Exemplary 3D class averages of NSP2-RNP with strong (boxed) and weak (all other) RNA density features.

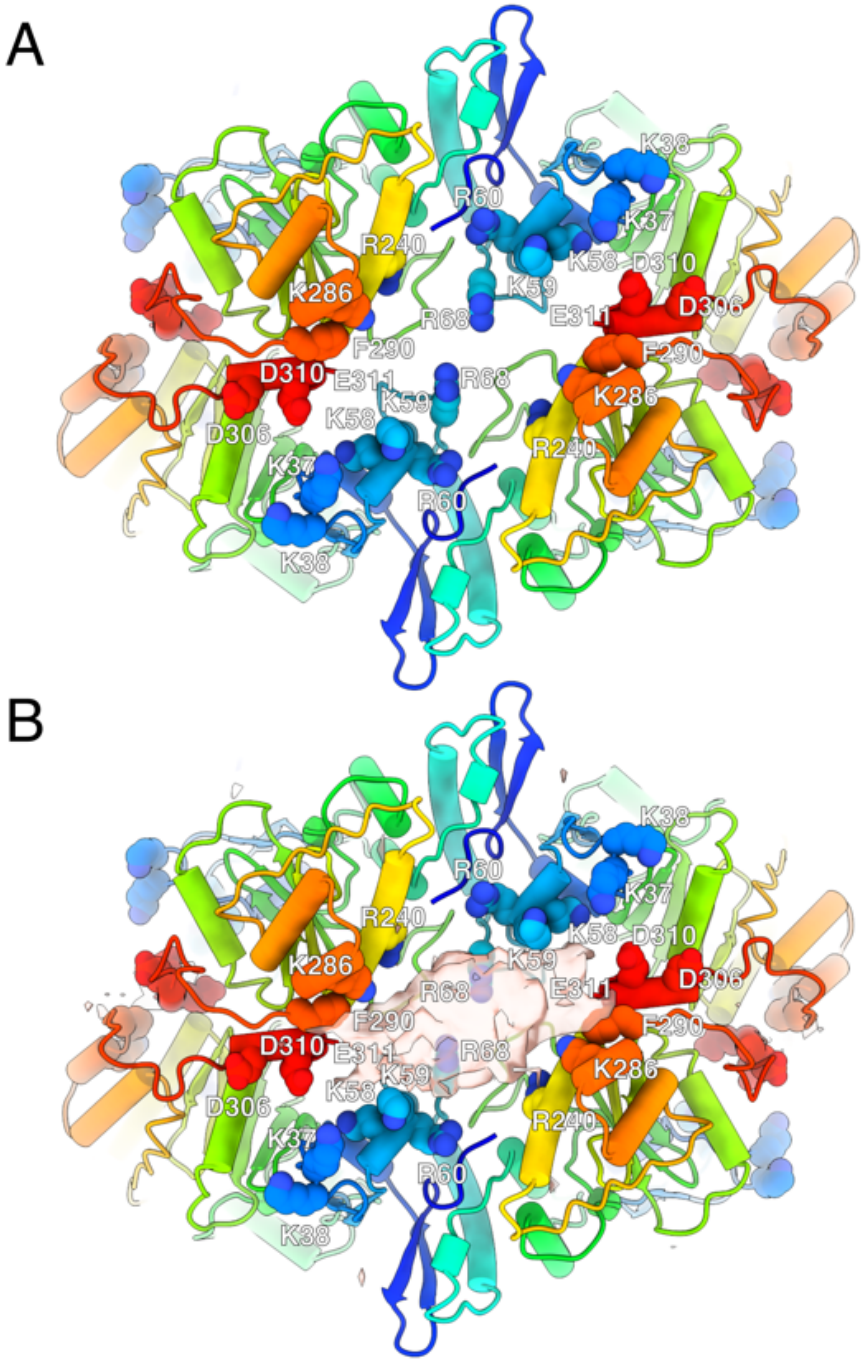

Supplementary Figure S9. Putative RNA-interacting residues. A: An atomic model of NSP2 with potential RNA-interacting residues & acidic residues within CTR (D306, D310, E311) shown as spheres. **B:** The model shown in A with the positive cryo-EM difference map (i.e. RNA density) superimposed.

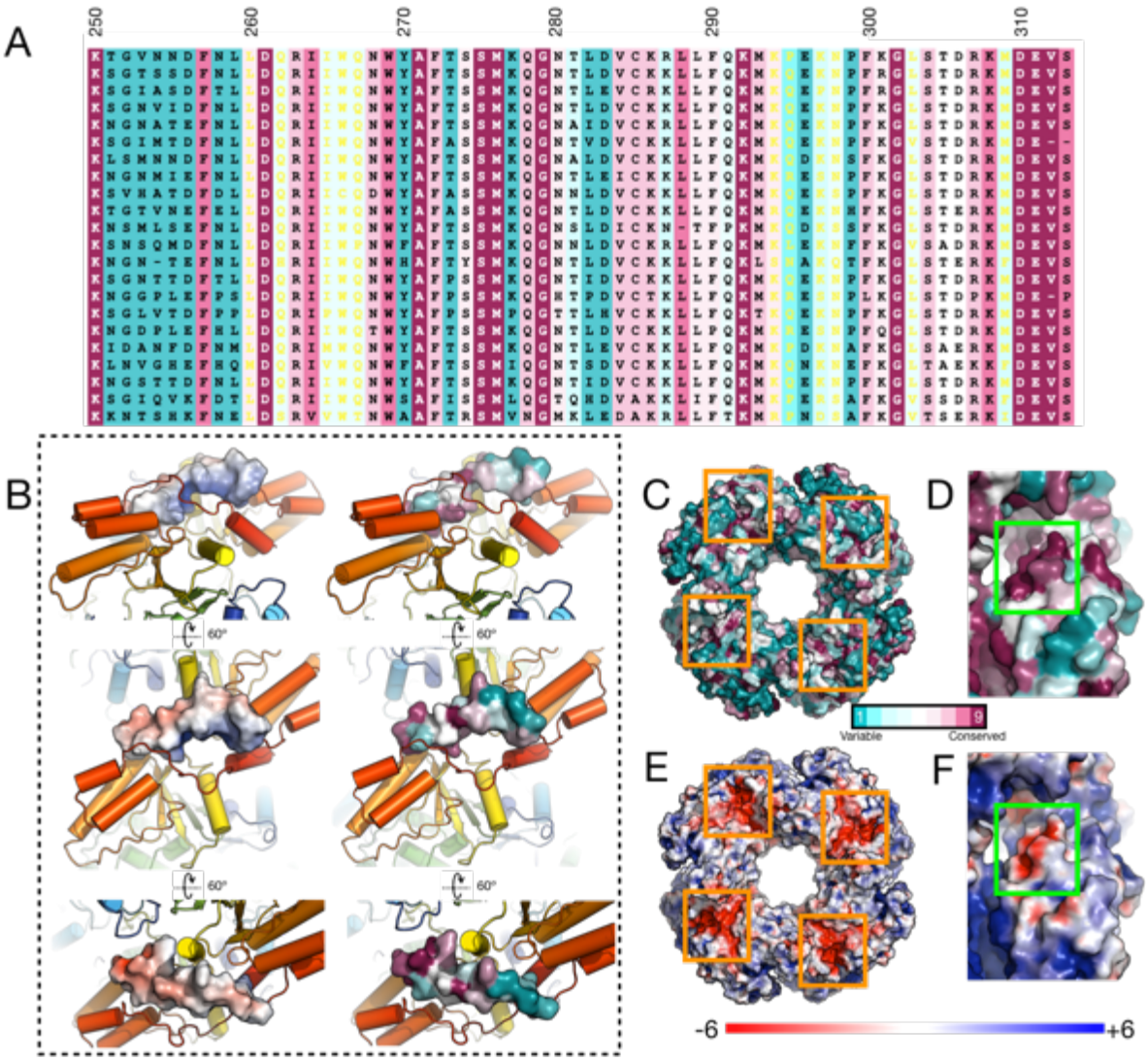

Supplementary Figure S10. Conservation & electrostatic analysis of NSP2. A: A ConSurf analysis of the NSP2 C-terminus (residues 250 – 313). **B:** Charge clusters patches are observable on alternate sides of the ampholytic NSP2 CTR surface. The cartoon representation of NSP2 is rainbow coloured according to sequence position. A single CTR is shown as a molecular surface structure. Left: ABPS surface. Right: ConSurf surface conservation surface. **C – F:** Surface-exposed acidic patches within the NSP2 with low (C & E, orange boxes) and high (D & F, green boxes) levels of sequence conservation, as calculated using ConSurf. The highly conserved acidic patch in D & F is within the CTR (D306, D310, E311).

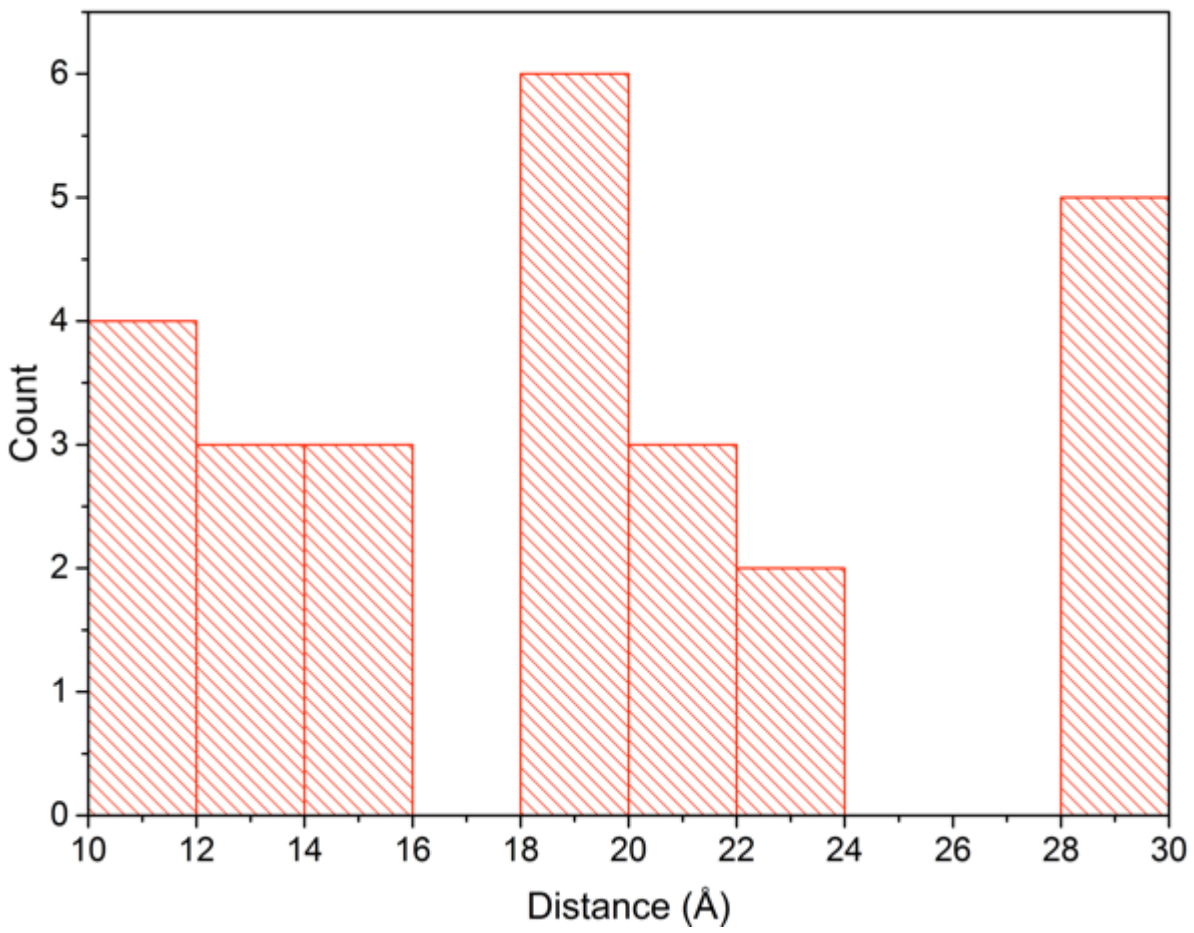

764

765 **Supplementary Figure S11. Distances between nearest CTR and cryo-EM-**
766 **identified RNA-binding residues (KKRR: K58, K59, R60, R68) and acidic residues**
767 **within the CTR (DDE: D306, D310, E311).** For the sake of clarity, only distances
768 between RNA-binding residues and CTR ≤ 30 Å were included. Distances were
769 measured using ChimeraX (*48*).

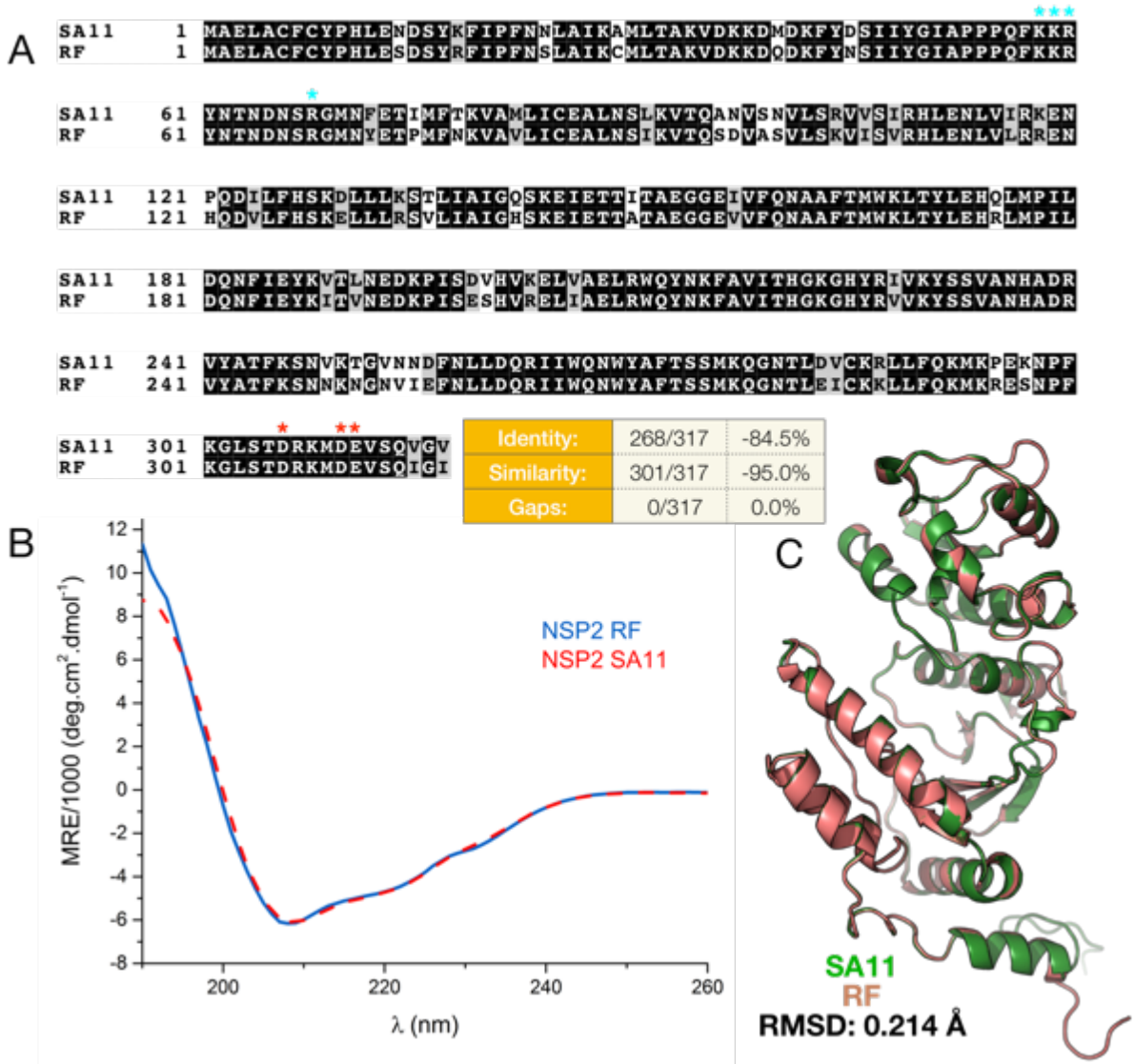

Supplementary Figure S12. The similarity of NSP2 encoded by the rotavirus strains RF and SA11. A: Alignment of the SA11 and RF NSP2 sequences. RNA-binding residues (as suggested by cryo-EM) are denoted with cyan asterisks. Residues constituting the CTR acidic patch are denoted with red asterisks. Alignment was generated using T-Coffee (*61*) **B**: Circular dichroism (CD) spectra of NSP2 RF (blue) and SA11 (red). **C**: The protein 3D structure prediction of NSP2 RF (pink) was determined using the threading approach using I-TASSER (*62*) based upon the SA11 crystal structure (green). These two atomic models are highly similar, with an overall RMSD between equivalent Cα atoms of the refined model presented here and PDB 1L9V of 0.214 Å.

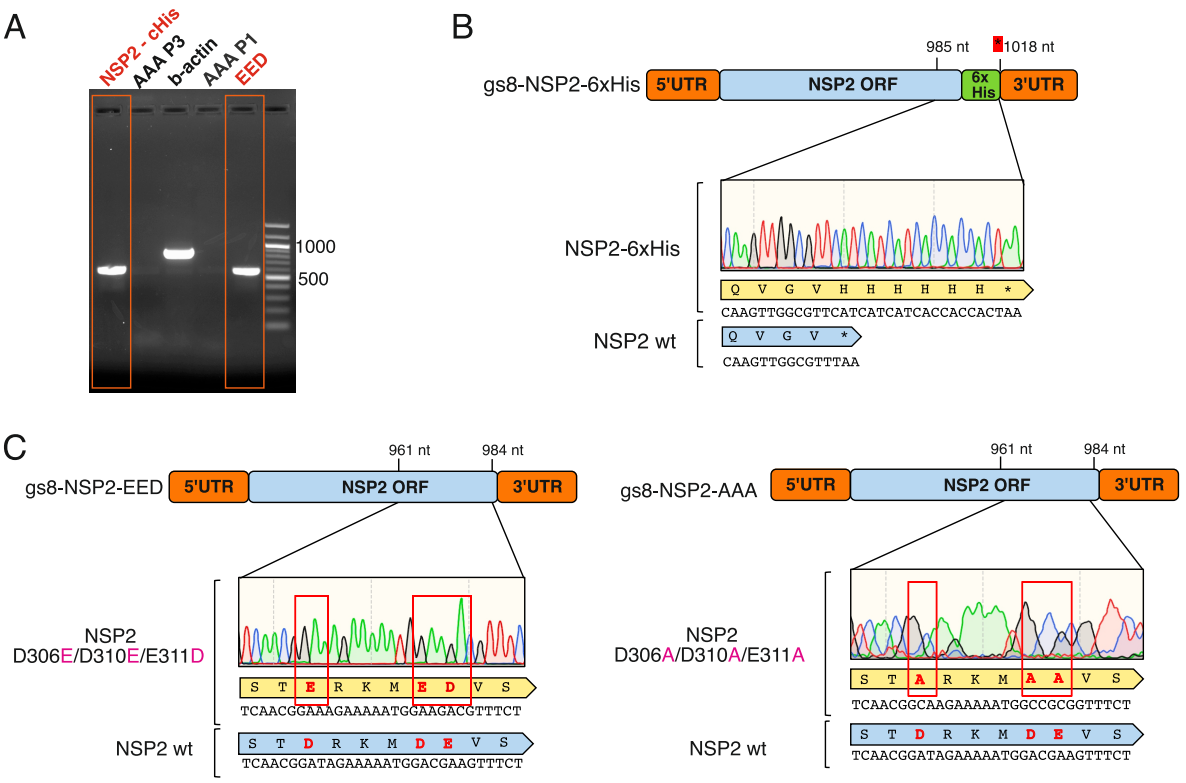

Supplementary Figure S13. Rescue of replication-competent NSP2 mutant rotaviruses in reverse genetics experiments. A. RT-PCR results of the RNA extracted from MA104 cells infected with lysates from reverse genetics experiments designed to rescue C-terminally 6xHis-tagged NSP2 (panel B), and NSP2-EED and NSP2-AAA mutants (panel C). For each experiment, three independent attempts were made to rescue the wild-type virus and the mutants. Total RNA was extracted from virus-infected cells for each mutant (Materials and Methods), and amplified using gs8-specific primers, prior to further verification by sequencing. For gs8-NSP2-AAA mutant, sequencing data are shown only for the plasmid gs8-NSP2-AAA used for the virus rescue, as no cDNA could be made due to the absence of replicating viral RNA, even after two blind passages (panel A, AAA mutant, lane P3).

796 **Supplementary Table S1. Sequences of RNAs used in the study**

RNA substrate	Sequence (5' – 3')
Unstructured 20mer (unlabeled) (used for RNA competition assay Fig. 7A)	CUUUUCAAGACAUGCAACAA
Unstructured 20mer (labelled) (used for RNA competition assay Fig. 7A)	AF488-CUUUUCAAGACAUGCAACAA
Unstructured 10mer (labelled) (used for peptide competition assay Fig. 7B)	AF488-CUUCUUUCGA
Biotinylated unstructured 10mer (SPR, Fig. 6)	Biotin-CUUCUUUCGA
Dual-labelled stem loop (smFRET, Fig. 3)	ATTO532-AAAUCUUUGCAAACUAUCCAAUCCAUGCAAAGAUAA-ATTO647N
40mer RNA (cryo-EM)	CUUUUCAAGACAUGCAACAACUUUUCAAGACAUGCAACAA
RV S5 (GenBank ID)	KF729657.1
RV S6 (GenBank ID)	KF729692.1
RV S11 (GenBank ID)	KF729697.1
Q5 SDM primers – NSP2-6xHis	FOR: ATGATGATGAACGCCAACTTGAGAAAC REV: CACCACCACTAATTCGCTATCAATTTGAG
Q5 SDM primers – NSP2-DEE	FOR: ATGGAAGACGTTTCTCAAGTTGGCGTTTAATTC REV: TTTTCTTTCCGTTGACAGCCCTTTAAATG
Q5 SDM primers – NSP2-AAA	FOR: ATGGCCGCGGTTTCTCAAGTTGGCGTTTAATTC REV: TTTTCTTGCCGTTGACAGCCCTTTAAATG
gs8-NSP2 sequencing/RT-PCR	FOR: GAAATCAACACTGATTGCTATTG REV: CCATCATCATCCTCAAATTG

797

798 **Supplementary Table S2 Cryo-EM data collection and refinement statistic**

	NSP2 apoprotein	NSP2 RNP
Data collection and processing		
Nominal Magnification	75,000	
Voltage (kV)	300 kV	
Defocus range (μm)	-1.2 to -2.4	-1.5 to -3.5
Detector	Falcon III	Gatan K2
Pixel size (Å)	1.065	1.07
Electron exposure (e^-/Å^2)	110	55
Symmetry imposed	D4	
Particles in first 3D classification	955,893	1,245,861
Final particle number	109,391	38,252
Nominal map resolution (Å)	3.90	3.14
B-factor*	-239.2	-100.8
FSC threshold	0.143	
Map resolution range (Å)	3.64 – 4.46	3.22 – 4.19
Refinement, model composition and validation		
Initial model used	PDB 1L9V	
Model resolution (Å)	4.0	3.2
FSC threshold	0.5	
Non-hydrogen atoms	20368	20368
RMSD bonds (Å)	0.004	0.008
RMSD angles (º)	0.651	0.810
Ramachandran		
Favoured (%)	92.52	93.01
Allowed (%)	7.48	6.99
Outliers (%)	0.00	0.00
Rotamer outliers (%)	0.00	0.00
Clash score	10.77	7.13
Molprobity score	2.02	1.84
Model-to-map fit		
Cross-correlation coefficient (mask)	0.82	0.83
Cross-correlation coefficient (volume)	0.81	0.81
Main-chain	0.81	0.83
Sidechain	0.78	0.81

799

800 **Supplementary Table S3 Binding kinetics of NSP2 and NSP2-ΔC as measured**
801 **by SPR.** The association (K_{on}) and dissociation (K_{off}) rate constants obtained by SPR
802 are given below.

RNA used	Sample	[NSP2] (nM)	K_{on} ($M^{-1}s^{-1}$)	K_{off} (s^{-1})	K_D (pM)	χ^2	ΔOFF**
10mer RNA	NSP2 WT	6.25	1.37×10^{6}	9.04×10^{-4}	6580	1.742	N/A
		12.5	6.71×10^{5}	8.58×10^{-4}	1280	15.23	
		25	5.12×10^{5}	7.20×10^{-4}	1410	128.7	
	NSP2 ΔC	6.25	8.24×10^{5}	2.92×10^{-4}	354	15.85	**3.10**
		12.5	4.03×10^{5}	2.40×10^{-4}	596	30.43	**3.58**
		25	4.95×10^{5}	2.46×10^{-4}	497	72.05	**2.93**

803